4-24-2012

Latent Heat Thermal Energy Storage with Embedded Heat Pipes for Concentrating Solar Power Applications

Christopher Robak
christopherrobak@gmail.com

Latent Heat Thermal Energy Storage with Embedded Heat Pipes for Concentrating Solar Power Applications

Christopher Walter Robak

B.S., University of Connecticut, 2009

A Thesis

Submitted in Partial Fulfillment of the

Requirements for the Degree of

Masters in Science

At the

University of Connecticut

2012

Certificate of Approval

Master of Science Thesis

Latent Heat Thermal Energy Storage with Embedded Heat Pipes for Concentrating Solar Power Applications

Presented by:

Christopher Walter Robak

Major Advisor 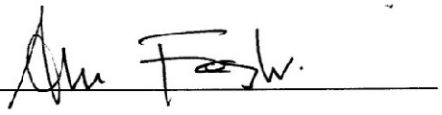

Amir Faghri

Co-Major Advisor 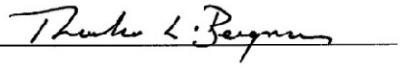

Theodore Bergman

Associate Advisor 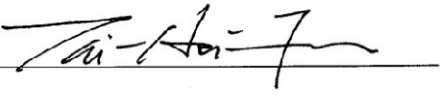

Tai-Hsi Fan

University of Connecticut

2012

Acknowledgements

I would like to take this opportunity to personally thank the individuals who have helped me during my master's thesis research. I have gained invaluable knowledge in science and engineering through the pursuit of this degree, which would not have been possible without the guidance of the people around me.

I would like to thank Dr. Faghri, my major advisor over the past 3 years, for offering me the opportunity to conduct research in the fields of thermal energy storage and heat pipe technology. Dr. Faghri has been a great mentor, teaching me how to be a good researcher, student, and leader in the laboratory. Without his help this would not have been possible.

I would like to acknowledge and thank my co-major advisory Dr. Bergman for his guidance with my research and for his contributions editing my journal publications. It is an honor to have worked with Dr. Bergman during my graduate career and I have learned many skills from him which I will continue to use as a practicing engineer.

During graduate school, I have had the pleasure to be a student in several of Dr. Fan's classes. He has been an excellent professor, and I would like to thank him for being an associate advisory on my thesis committee.

To my fellow lab mates, thank you for your help, support and guidance with my school and research efforts. Everyone has been a wonderful friend and colleague and I will miss working with you. I would also like to thank my family and friends for their understanding, encouragement, and support throughout my college career.

Lastly, financial support from the U.S. Department of Energy and the U.S. Department of Education is gratefully acknowledged.

Table of Contents

List of Figures

List of Tables

Abstract

An innovative, novel concept of combining heat pipes with latent heat thermal energy storage (LHTES) for concentrating solar power (CSP) applications is explored. The low thermal conductivity of phase change materials (PCMs) used in LHTES presents a design challenge due to slow heat transfer rates during heating and cooling of the material. Heat pipes act to decrease the thermal resistance in the PCM, increasing the overall heat transfer rate sufficiently for use in CSP. First, a laboratory scale experiment is presented to validate the concept of using heat pipes in LHTES to reduce thermal resistance in PCM. A commercial scale LHTES with embedded gravity assisted heat pipes is then modeled and a cost analysis is conducted to determine competitiveness with other forms of thermal energy storage currently used in the CSP industry.

LHTES utilizing heat pipes or fins is investigated experimentally. Photographic observations, melting and solidification rates, and PCM energy storage quantities are reported. A variable, heat pipe effectiveness, is defined and used to quantify the relative performance of heat pipe-assisted and fin-assisted configurations to situations involving neither heat pipes nor fins. For the experimental conditions of this study, inclusion of heat pipes increases PCM melting rates by approximately 60%, while the fins are not as effective. During solidification, the heat pipe-assisted configuration transfers approximately twice the energy between a heat transfer fluid and the PCM, relative to both the fin-assisted LHTES and the non-heat pipe, non-fin configurations.

Secondly, an economic evaluation of a LHTES system for large scale CSP applications is conducted. The concept of embedding gravity-assisted wickless heat pipes (thermosyphons) within a commercial-scale LHTES system is explored through use

of a thermal network model. A new design is proposed for charging and discharging a large-scale LHTES system. The size and cost of the LHTES system is estimated and compared with a two-tank sensible heat energy storage (SHTES) system. The results suggest that LHTES with embedded thermosyphons is economically competitive with current SHTES technology, with the potential to reduce capital costs by at least 15%. Further investigation of different PCMs, thermosyphon working fluids, and system configurations has the potential to lead to designs that can further reduce capital costs beyond those reported in this study.

Key Words: Concentrating Solar Power, Latent Heat, Thermal Energy Storage, Heat Pipe, Phase Change Material

Chapter 1. Introduction

1.1. Introduction

Interest in concentrating solar power (CSP) has increased as the demand for renewable sources of energy continues to grow. CSP technology utilizes concentrated solar radiation to drive a heat engine, generating electricity. Several types of CSP designs include solar power towers, parabolic troughs, Fresnel reflectors, and Stirling dish engines (Madaeni et al., 2011). Modern solar power towers and parabolic trough collectors can reach temperatures in excess of 600 ºC, with future plans to increase the operating temperature above 800 ºC.

Figure 1.1 shows a simple schematic for a parabolic trough type CSP installation. Solar radiation is concentrated by parabolic collection mirrors onto a focal point, where it heats a heat transfer fluid (HTF) flowing through a tube. As the HTF passes through the solar field, it gains thermal energy, becoming hot. The hot HTF is then passed through a heat exchanger, delivering the captured thermal energy to a power cycle for electricity production. A portion of the hot HTF can be transferred to thermal energy storage (TES) for use during times of low or no solar radiation. Fresnel reflectors and solar power towers employ different methods to concentrate solar radiation, but are similar in operation to parabolic trough systems. Stirling dish engines are more compact than the other CSP technologies and generate power in smaller units using a Stirling power cycle.

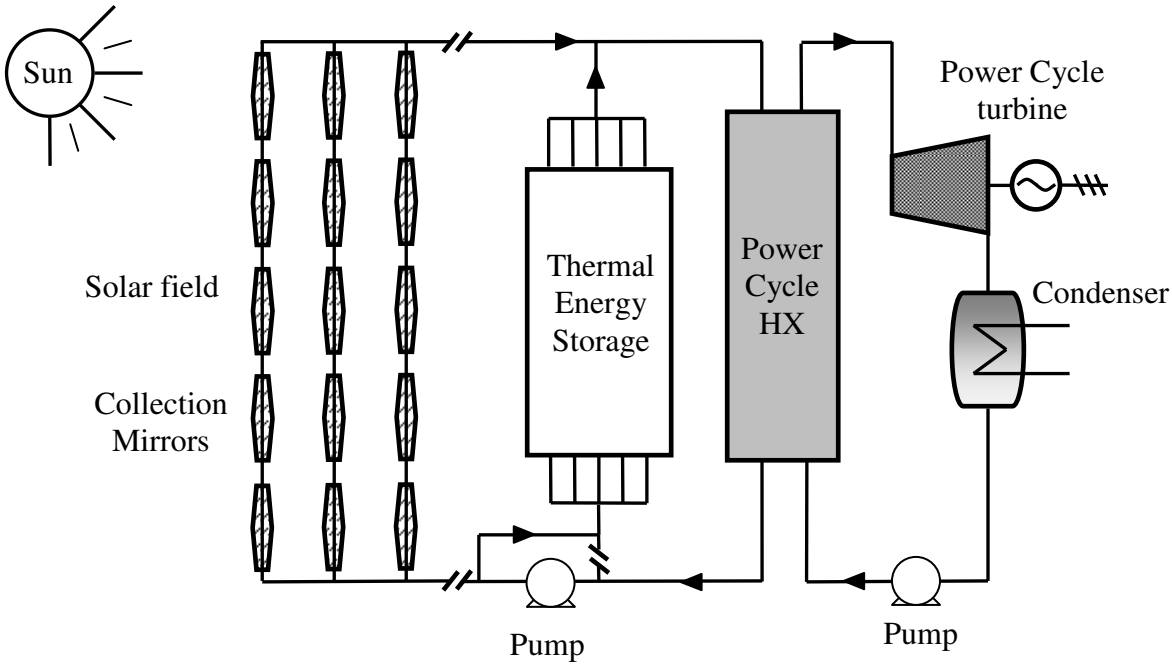

Figure 1.1: Conceptual diagram of a parabolic trough CSP plant

CSP technology has already been demonstrated in the southwest portion of the United States. As early as 1984, Luz International Limited constructed parabolic trough CSP plants in California as part of the solar electric generation system (SEGS) project. By 1991, 9 SEGS CSP plants had been constructed, representing 348 MW_e capacity (Mills, 2004). In general, the relatively high cost of CSP has made construction of additional plants economically unattractive. Recently, however, several new CSP projects have been proposed both in the United States and Europe, with an increased expectation that TES can reduce costs associated with this form of electric power production (Mills, 2004).

Thermal energy storage can reduce the cost CSP-generated electric power net cost, mainly in two ways. First, TES-enabled power leveling decreases the size of the components of the power block, reducing capital and construction costs. Second, TES allows shifting power production to times of higher demand so the power can be sold at a higher price. Thermal energy storage can also make CSP plants more "dispatchable" by allowing plant operators to supply electricity during times of high electric demand, while storing excess thermal energy when demand is low. This is advantageous over other forms of renewable energy, such as photovoltaic cells and wind turbines, which directly generate electricity, and cannot be easily controlled. Although it is possible to store electrical energy, it is generally more expensive than TES with higher round trip efficiency losses (Madaeni et al., 2011).

Currently, sensible heat thermal energy storage (SHTES) technology is the only large scale method for storing solar thermal energy for CSP; the two-tank molten salt SHTES is the standard CSP TES technology. Two-tank SHTES works by heating an

energy storage material, usually a molten nitrate salt mixture, from a low temperature to a high temperature. The low temperature molten salt is initially stored in a cold tank. During daytime operation, the cold molten salt is heated with excess solar thermal energy and then pumped to a hot storage tank. The hot salt is utilized to extend the operational time of the CSP plant at night. As the energy is extracted from the hot salt, it is passed back into the cold tank and the cycle is repeated.

SHTES has been proven to reduce CSP capital costs, and as a result several new CSP installations, most notably the Andasol 1 plant in Spain, have implemented SHTES. Disadvantages of SHTES are the large amount of medium (salt) required to store the thermal energy (and the two correspondingly large storage tanks), as well as potentially detrimental solidification of the salt if the temperature within the storage tanks drops below the salt's solidification point (Mills, 2004). Additionally, the nitrate salt mixtures used in most modern SHTES systems is unstable above 650 ºC, which limits the maximum storage temperature and correspondingly the power cycle efficiency in higher temperature CSP applications.

Interest in alternative TES methods has evolved in order to further improve the technology. Latent heat thermal energy storage (LHTES) is of particular interest because it stores thermal energy primarily due to solid-liquid phase changes and, when materials having a high heat of fusion are used, it requires less storage material relative to SHTES, reducing capital and construction costs. Because LHTES is designed to undergo melting and solidification during sequential charging and discharging processes within a single storage unit, it obviates the need for two separate tanks and the freezing problem encountered by two-tank SHTES. Additionally, the use of a materials latent heat of

fusion to store energy means that a smaller temperature gradient is required for heat transfer, since a material absorbs large amounts of thermal energy at its melting point. The primary disadvantage of LHTES is the low thermal conductivity that characterizes many phase change materials (PCMs), leading to potentially slow discharging and charging rates, as well as a reduced thermodynamic efficiency (low maximum cycle temperatures) of the CSP power block. As such, much research involving LHTES has been aimed at circumventing the high thermal resistance posed by the PCM.

Several LHTES designs for small-scale, low temperature applications have been considered by Medrano et al. (2009). They tested different heat exchanger designs to reduce the thermal resistance of the LHTES. It was concluded that a double-pipe PCM - HTF heat exchanger with an embedded graphite matrix worked well for low temperature, paraffin-based PCMs. A higher temperature LHTES unit was proposed by Laing et al. (2011) for a commercial scale CSP operation using direct steam generation. Their research involved the design and testing of a LHTES using sodium nitrate as the PCM that was, in turn, enclosed in a vertically-oriented tank with hexagonal finned tubes carrying liquid water. In this particular design the water, pressurized to 100 bars, is vaporized in the LHTES unit to create steam for electric power production. A 1 MWh system was successfully constructed and field-tested. However, since most large scale CSP designs utilize an organic fluid to transfer energy to and from the solar field, the direct steam LHTES unit proposed by Laing et al. (2011) might need to be modified for widespread CSP use.

To reiterate, the largest barrier to the development of large scale LHTES is the low thermal conductivity of most phase change materials (PCMs) and much of the

previous research regarding LHTES has focused on reducing the thermal resistance posed by the PCM. For example, Velraj et al. (1999) incorporated Lessing rings within PCM and observed increased heat transfer rates from the PCM to a coolant, making the technique suitable for reducing solidification times. The investigators also considered use of extended surfaces to increase heat transfer, concluding that fins also reduce total solidification times by approximately 75% based upon the predictions of a numerical model. Similar results for LHTES melting (charging) experiments utilizing a finned heat transfer fluid (HTF) tube have been reported by Balikowski and Mollendorf (2007). Sparrow et al. (1981) showed that small fins can triple the amount of PCM that freezes about a cold tube. In other work, Agyenim et al. (2010) demonstrated that faster PCM heating can be achieved by increasing the number of heat transfer tubes embedded in a PCM. Although the preceding approaches increase heat transfer rates in LHTES systems, they all occupy volume within the PCM storage vessel. Ideally, any strategy to increase heat transfer rates would also occupy little space in order to maximize energy storage capacity.

In this thesis, incorporation of heat pipes with LHTES is of interest. Heat pipes are simple, passive devices that are able to transfer large quantities of thermal energy from one end to another with little temperature gradient. In general, heat pipes consist of a hollow metallic tube, sealed at both ends. The interior of the tube contains a wick structure and a working fluid under a vacuum environment. When heat is applied to one end of a heat pipe, the working fluid contained within begins to boil, since it is under vacuum. This portion of the heat pipe is called the evaporator, since the thermal energy applied is transferred into the working fluid through latent heat of vaporization. The

vaporized working fluid then travels up the interior of the heat pipe, until it reaches the opposing end, called the condenser. At the condenser, the vaporized working fluid condenses on the interior wall, releasing its latent heat of fusion. The condensed working fluid can travel back to the evaporator by means of gravity or capillary action in the wick structure. Figure 1.2 diagrams of the operation of a heat pipe.

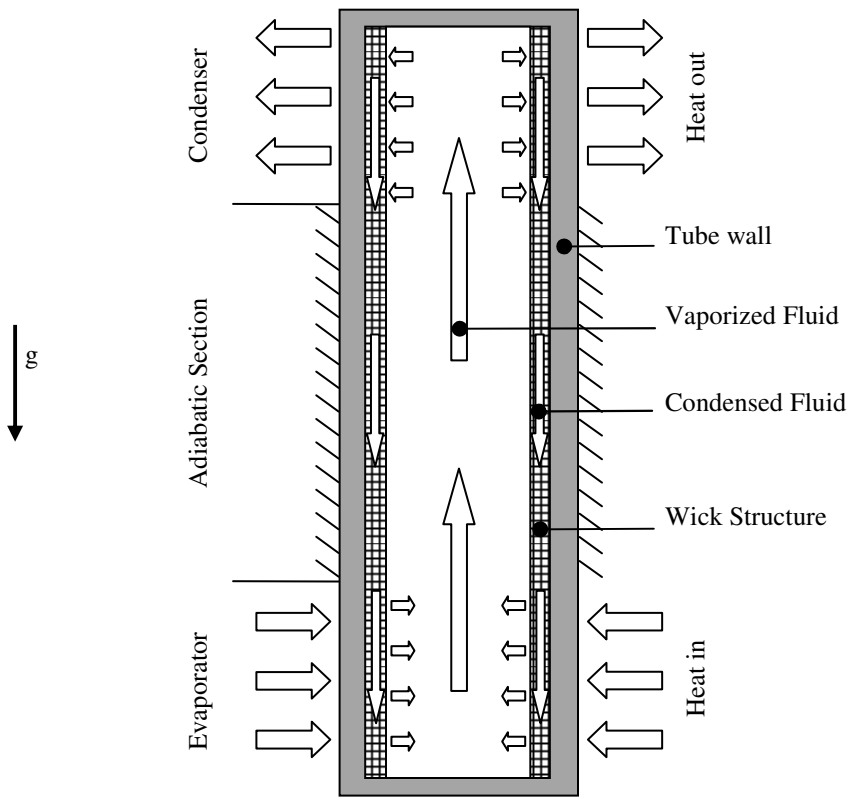

Figure 1.2: Operational diagram of a heat pipe

Since heat pipes transfer heat using the latent heat of vaporization of the working fluid, they can transfer large quantities of heat at nearly isothermal conditions. In fact, the effective thermal conductivities of some common copper-water heat pipes used in electronic cooling applications are approximately 90 times greater than copper rods of the same dimensions (Faghri, 1995).

Heat pipes may be utilized to increase heat transfer rates to or from the PCM, while maintaining small temperature differences between the PCM and HTF. Limited research regarding heat pipe-assisted LHTES has been conducted. Faghri (1990, 1991) holds two U.S. patents that describe the use of miniature heat pipes in small LHTES modules. Experimentally, Lee et al. (2006) developed a low temperature LHTES system operating with a variety of PCMs that utilized a two-phase thermosyphon operating with ethyl alcohol as the working fluid. A paraffin LHTES, with copper-water heat pipes embedded within a rectangular PCM enclosure, was developed and tested by Liu et al. (2005). Recently, Shabgard et al. (2010) modeled a large scale heat pipe-assisted LHTES and reported predictions showing improvement in both melting and solidification rates.

The research conducted for this thesis is meant to further demonstrate the novel idea of embedding heat pipes into PCM to decrease thermal resistance. Specifically, the goal is to show that LHTES can be made competitive with modern SHTES from a heat transfer and economic perspective for CSP applications. Chapter two will discuss a low (room) temperature experiment involving a heat pipe-PCM system, quantifying the impact heat pipes have on the melting and solidification process during a charging-discharging cycle. Chapter three takes a more conceptual approach to heat pipe-PCM

LHTES, developing a heat transfer model for a large scale system and evaluating the economics of LHTES relative to modern SHTES.

Chapter 2. Experimental Investigation

2.1. Motivation

Although some research has been conducted regarding heat pipe-assisted LHTES, the effectiveness of the approach has apparently not been quantified experimentally. Therefore, the objective here is to experimentally establish the effectiveness of heat pipes in potentially increasing heat transfer rates in a LHTES system by directly comparing measured performance with: (*i*) a system with no heat pipes, and (*ii*) a system utilizing fins in lieu of heat pipes. Results are reported for both melting (charging the LHTES system) and solidification (discharging).

2.2. Experimental Design

A paraffin, n-octadecane ($C_{18}H_{38}$, T_m = 27.5ºC) of 99% purity, the properties of which are listed in Table 2.1, was used as the PCM. This material was selected because it is stable and non-toxic, and will not cause corrosion. Moreover, the thermophysical properties of n-octadecane are well-established and the material has a transparent liquid phase, permitting visual observation of melting and solidification phenomena. As is well known, this material has been used extensively as an experimental, low-temperature PCM (Balikowki and Mollendorf, 2007; Bathelt and Viskanta, 1980; Choi and Hong, 1990; Hale and Viskanta, 1978,1980; Ho and Viskanta, 1984; Ju et al., 1998; Lacroix, 1993).

Table 2.1: Thermophysical properties of n-octadecane.

Property	Value
Melting point[a]	$T_m = 27.5$ºC
Latent heat of fusion[a]	$\lambda = 243.5$ kJ/kg
Liquid density[b]	$\rho_\ell = 770$ kg/m^3
Liquid specific heat[b]	$c_{p,\ell} = 2160$ J/kg·K
Liquid thermal conductivity[a]	$k_\ell = 0.148$ W/m·K
Liquid thermal diffusivity[a]	$\alpha_\ell = 8.64 \times 10^{-8}$ m^2/s
Kinematic viscosity[a]	$\nu = 4.013 \times 10^{-6}$ m^2/s
Liquid thermal expansion coefficient[a]	$\beta_\ell = 0.0009$ K^{-1}
Solid density[b]	$\rho_s = 800$ kg/m^3
Solid specific heat[c]	$c_{p,s} = 1912$ J/kg·K
Solid thermal conductivity[a]	$k_s = 0.358$ W/m·K
Solid thermal diffusivity[a]	$\alpha_s = 2.14 \times 10^{-7}$ m^2/s

[a] (Lacroix, 1993)
[b] (Balikowski and Mollendorf, 2007)
[c] (Fukai et al., 2000)

Note: Minor differences exist between properties from various sources.

An overall schematic of the experimental apparatus is shown in Fig. 2.1a. As shown in Fig. 2.1b, the test cell consists of a vertical, cylindrical PCM enclosure and underlying heat exchanger. The acrylic enclosure has an inside diameter of 127 mm, a height of 200 mm, and a wall thickness of 6 mm. It is mounted to a heat exchanger that serves as the heat source (sink) for melting (solidification). The cylinder is mated to the heat exchanger by way of a 7-mm wide, 4-mm deep channel housing a synthetic rubber **O**-ring.

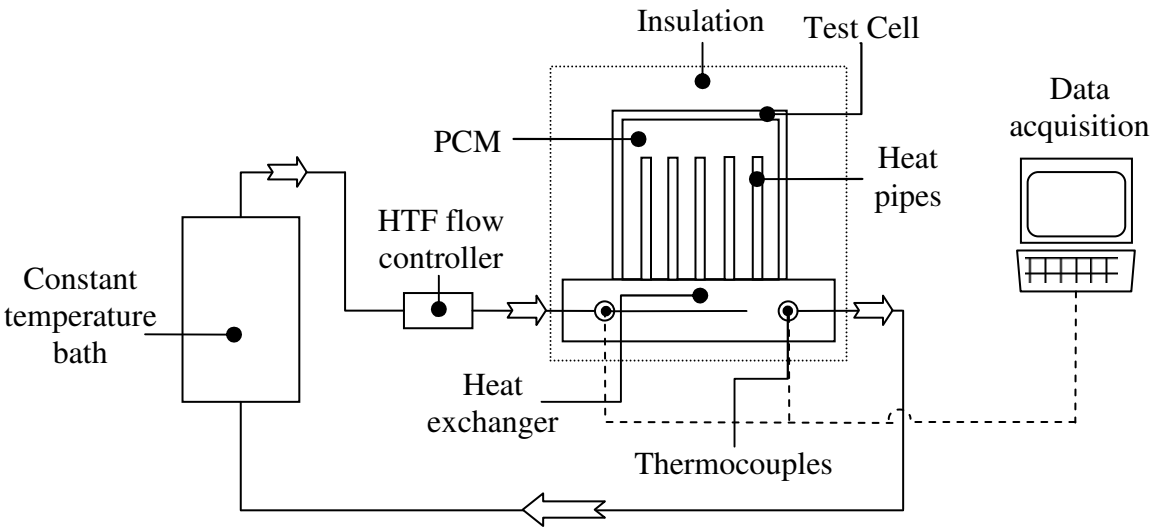

(a)

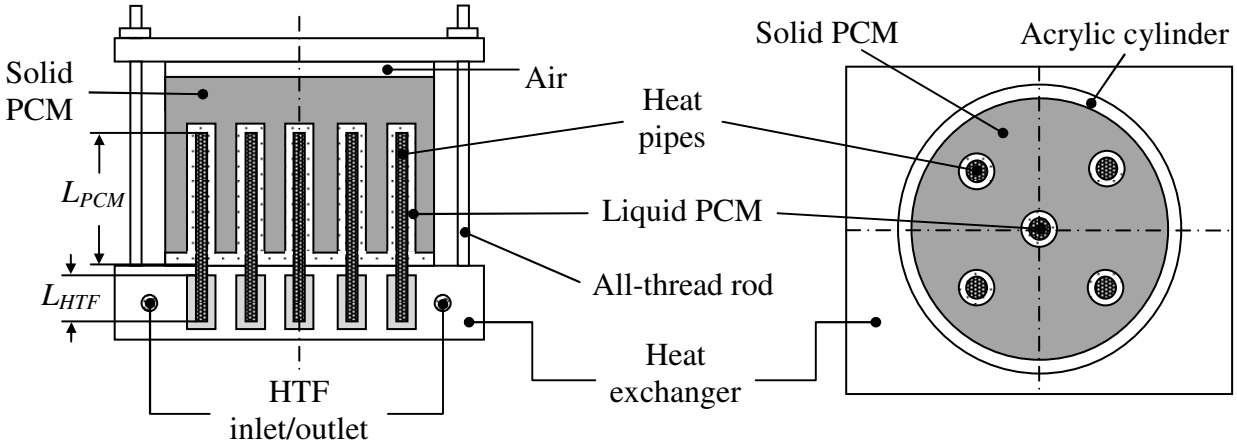

(b)

Figure 2.1: (a) Schematic of overall experimental setup. (b) Detailed diagram.

Two heat exchangers were utilized, the first with a plane top surface for benchmark experiments involving neither heat pipes nor fins. The bottom section of the heat exchanger was constructed of an aluminum (6061) block of length 203 mm, width 187 mm, and thickness 52 mm. HTF flow channels of width 9.4 mm and depth 40 mm were milled into the block in a serpentine pattern. A 6-mm thick aluminum top plate was attached to the block to complete the heat exchanger assembly. The top of the test cell cylinder was covered with an aluminum plate using a similar **O**-ring sealing arrangement as described previously. Leaks were prevented by compressing the **O**-rings with four all-threaded rods, as shown in Fig. 2.1b. The entire test cell was insulated with a box made from 37-mm thick extruded polystyrene board lined with Fiberfrax ceramic insulation.

The second heat exchanger incorporated a top plate that was modified to accommodate heat pipes or fins. Specifically, five 13-mm diameter threaded holes accepted Swagelok fittings that were, in turn, used to secure either heat pipes or fins that penetrated through the top plate. Five 175-mm long, 6-mm outer diameter copper-water heat pipes (Enertron, model HP-HD06DI17500BA) were installed during the heat pipe-assisted experiments. One heat pipe was centered in the cylindrical test cell, while four heat pipes were mounted in a square pattern, 37 mm from the centerline. During charging or discharging L_{HTF} = 40 mm sections of the heat pipes were inserted within the HTF flow channels, in direct contact with the HTF. Heat pipe lengths of L_{PCM} = 129 mm were exposed to the PCM. For experiments involving fins, the heat pipes were replaced with 316 stainless steel rods of the same dimensions. The low thermal conductivity fin material was specified in order to achieve a fin efficiency similar to that which might be

expected in a large scale LHTES system incorporating high thermal conductivity fins (see Appendix 2.A).

Distilled water was used as the HTF, its temperature regulated by a RM 5 Lauda constant temperature bath to within an accuracy of ± 0.1ºC of the set point. The HTF flow rate was set using an Omega FLV-4605A 0-2 LPM calibrated flow controller, with a manufacturer-reported accuracy of ± 0.0007 kg/s. However, for each experiment the flow rate was independently determined using a simple weight-over-time method and the variation during the course of a single experiment was found to be ± 0.0001 kg/s. Four Teflon-coated, 254 μm diameter chromel-alumel (K-type) thermocouples were installed within the HTF at both the inlet and the outlet of the heat exchanger. In addition, a vertical thermocouple rake with four 254 μm, K-type thermocouples positioned 20, 40, 60, and 80 mm from the heat exchanger was installed in the PCM to monitor its temperature during the solidification experiments. Calibration of all thermocouples was performed at both the freezing and boiling points of water, and the estimated thermocouple error is ± 0.1ºC. As will become evident, temperature differences were utilized for data reduction, and to minimize bias error all thermocouples were constructed from the same spool of wire. Thermocouple voltages were measured using a National Instruments data acquisition system.

The uncertainty in the HTF enthalpy change (from the inlet to the exit of the heat exchanger) was calculated using the sequential perturbation method (Figliola and Beasley, 2006), yielding uncertainties between ± 6 to 10% of the measured enthalpy difference. To quantify the uncertainty in melting and solidification rates, reproducibility

trials were conducted for both charging and discharging experiments, from which 90% confidence intervals were calculated using small-sample statistics.

2.3. Experimental Procedure

2.3.1 Charging

Melting experiments were conducted for benchmark cases involving neither heat pipes nor fins, for heat pipe-assisted charging, and for fin-assisted charging. The HTF flow rate was set to $\dot{m}_{HTF}$ = 0.0026 kg/s and inlet temperatures of either $T_{HTF,in}$ = 45ºC or 55ºC were employed. HTF inlet temperatures were selected to provide sufficient temperature difference between the HTF and the PCM while the HTF flow rate was specified to minimize the measurement error of the temperature drop through the heat exchanger. The PCM mass was approximately 1 kg in each experiment. The amount of total PCM used was measured to within ± 0.3 g.

The charging experiments involved a uniformly-solid PCM, relatively free of internal voids and air pockets. This was achieved by initially melting the PCM under vacuum, removing dissolved air from the PCM. Approximately 0.10 kg of de-gassed liquid PCM was added to the test cell as HTF at $T_{HTF} \approx 2$ ºC was circulated through the heat exchanger to induce solidification. After the initial layer of PCM solidified, another 0.10 kg of liquid PCM was added. The filling process continued in a layer-by-layer manner until the desired mass of PCM was in the test cell, after which circulation of the cold HTF was curtailed and the entire apparatus was allowed to equilibrate to room temperature ($T_\infty \approx 24$ºC) for at least 12 h. Using a two-dimensional conduction analysis (Bergman et al., 2011), it was estimated that the initial temperature of the PCM is $T_{i,c}$ =

24 ± 2ºC. The rather involved PCM filling and conditioning process limited the total number of experiments that were performed.

To compensate for unavoidable variations in the ambient temperature, HTF at $T_{HTF,in}$ = 26ºC was circulated in the heat exchanger prior to the start of each experiment. Subsequently, the flow of HTF to the heat exchanger was terminated and the set point of the water bath was increased to the desired level. Once the water temperature reached the set point, the heat exchanger was re-connected and the HTF flow controller was adjusted to the desired flow rate, marking the start of an experiment. Temperature and flow rate data were acquired at intervals of Δt = 5 s. The insulation was periodically removed and photographs were taken at intervals of approximately 30 min. Each charging experiment concluded when the PCM melted completely.

2.3.2 Discharging

Solidification experiments began with liquid PCM. Approximately 1 kg of n-octadecane was melted in the vacuum flask and then poured into the test cell. Using the constant temperature bath, warm HTF was circulated through the heat exchanger until thermocouples on the vertical rake within the PCM (between the two heat pipes to the right of the centerline in Fig. 2.1b) all indicated $T_{i,dc}$ = 43 ± 1ºC. The heat exchanger was disconnected and attached to a second Lauda bath at $T_{HTF,in}$ = 10ºC to mark the start of the experiment.

Discharging experiments were all conducted with a HTF temperature and flow rate of $T_{HTF,in}$ = 10ºC and $\dot{m}_{HTF}$ = 0.0022 kg/s, respectively. A limited number of experiments were performed since each experiment consisted of sub-experiments of

duration 30, 60, 90, 120, 180, and 240 min. That is, 6 separate tests were conducted for each experimental condition in order to accurately measure the amount of solidified PCM at discrete times. To do so, liquid PCM was siphoned from the test cell and weighed; photographs were also taken at the end of each sub-experiment. The thickness of solid PCM layers that formed on the heat exchanger surface and along the heat pipes (or fins) was measured with a caliper to an accuracy of ± 0.1 mm at the end of each sub-experiment. (The sub-experiment approach was not used during charging since it would have prolonged an already lengthy PCM filling and conditioning process.)

2.4. Results and Discussion

2.4.1. Charging Operation

Photographs of the melting process associated with the benchmark, heat pipe-assisted, and fin-assisted configurations with $T_{HTF,in}$ = 45ºC and a flow rate of $\dot{m}_{HTF}$ = 0.0026 kg/s are shown in Fig. 2.2. Three melting regimes are evident in the benchmark case (left column): conduction-dominated melting, natural convection-dominated melting, and contact melting (not shown). Immediately following the start of the experiment, warm temperatures diffuse upward within the PCM, leading to an initially planar melting front. The duration of conduction-dominated melting may be estimated by evaluating the critical Rayleigh number associated with the onset of free convection, Ra_{crit} = 1708 (Bergman et al., 2011), which for the conditions of the experiment corresponds to a liquid layer height of $H_\ell \approx 3$ mm. Using the Stefan solution (Bergman et al., 2011), it may therefore be shown that conduction-dominated melting exists only within the first few minutes of any experiment. Slight variations in liquid layer thickness

at t = 60 min (Fig. 2.2a) are attributed to (nominally) equally-spaced convection cells, consistent with observations made in similar experiments (Hale and Viskanta, 1980). As the solid-liquid interface propagates upward, the convection transitions to a turbulent mode, smoothing the solid-liquid interface (Fig. 2.2c). Toward the end of the experiment, $t \approx 250$ min, the solid PCM detached from the side walls of the test cell and sank to the bottom of the vessel, initiating close contact melting (not shown).

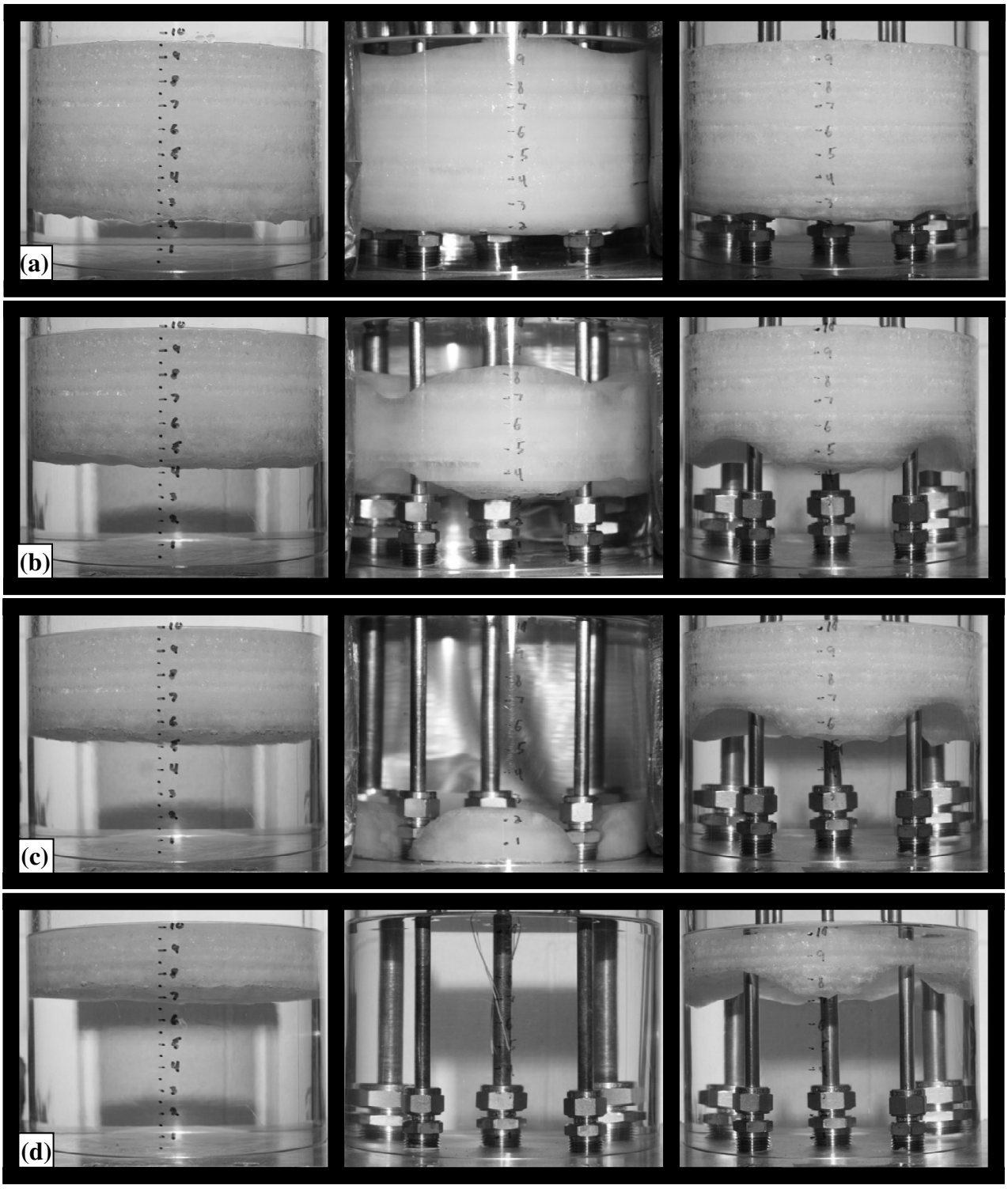

Figure 2.2: Temporal evolution of melting for the benchmark (left), heat pipe-assisted (middle) and fin-assisted (right) cases. (a) t = 60 min, (b) t = 120 min, (c) t = 150 min, (d) t = 210 min, ($T_{HTF,\,in}$ = 45ºC, $\dot{m}_{HTF}$ = 0.0026 kg/s, vertical scale in units of cm).

Heat pipe-assisted charging (middle column) markedly affects the shape, number, and propagation of multiple solid-liquid interfaces. At t = 60 min (Fig. 2.2a), the heat pipe-assisted and benchmark experiments display similar characteristics in the lower regions of the test cell. However, secondary melt fronts become established around the periphery of the warm heat pipes, evident in Fig. 2.3a at $t \approx 90$ min. The secondary fronts provide pathways for molten PCM, which is of lower density than the solid, to flow to the top of the test cell, feeding the tertiary, downward-propagating melting process, evident in Fig. 2.2b (and to an extent Fig. 2.2a). The heat pipes also induce a wavy, lower melt front along the test cell wall, evident at $t \approx 120$ min. This is attributed to the nearly isothermal heat pipe serving as a source of buoyancy in the molten PCM, causing secondary natural convection circulations. As in the benchmark case, the suspended solid eventually detached from the sides of the test cell, resulting in close contact melting shown in Fig. 2.2c. Complete melting is evident at t = 210 min (Fig. 2.2d).

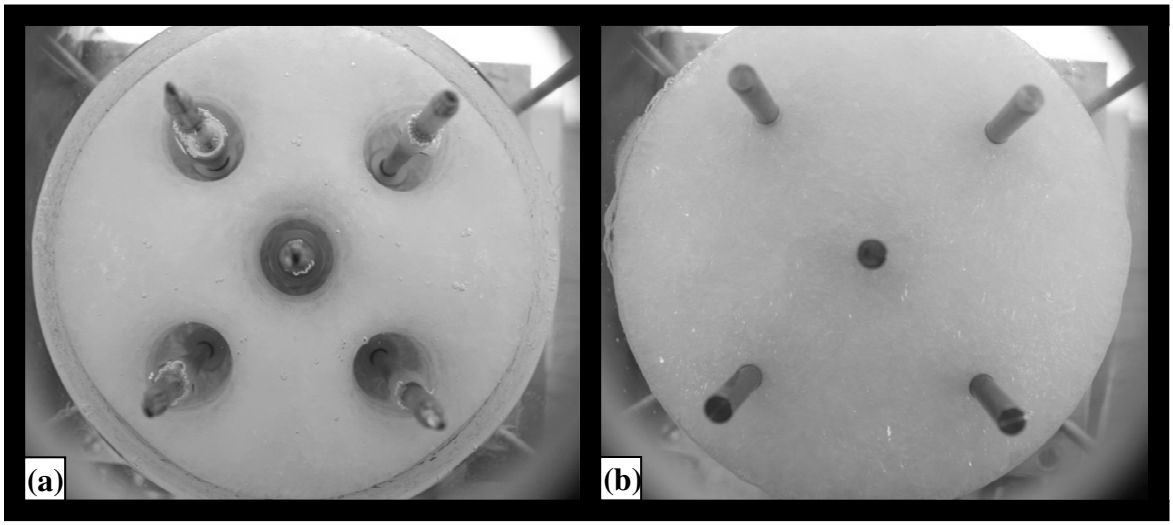

Figure 2.3: Top view of secondary melting (a) heat pipe-assisted charging, (b) fin-assisted charging (t = 90 min., $T_{HTF,in}$ = 45ºC, $\dot{m}_{HTF}$ = 0.0026 kg/s).

Fin-assisted melting (right column) exhibits features similar to those of the benchmark, with the exception of waviness in the melt front along the wall of the test cell in the vicinity of the fins, such as at $t \approx 120$ min (Fig. 2.2b). As in the heat pipe experiments, the waviness is attributed to fin-induced modifications in the natural convection circulation. Unlike the heat pipe-assisted experiments, however, localized melting did not occur around the top peripheries of the fins, as shown in Fig. 2.3b. Hence, liquid PCM was not provided with a pathway to the top of the solid PCM and no tertiary melting ensued, slowing the overall rate of melting relative to that of the heat pipe-assisted configuration.

The top portion of Table 2.2 includes melting rates, averaged over the duration of the various experiments, for the $T_{HTF,in} = 45$ºC conditions. These rates were determined by dividing the total PCM mass by the total melting times of 267 min, 157 min, and 232 min for the benchmark, heat pipe-assisted, and fin-assisted configurations, respectively. As evident, inclusion of heat pipes (fins) increased the average melting rates by 68% (13%).

Table 2.2: Average melting rates for benchmark, heat pipe-assisted, and fin-assisted melting for $T_{HTF,in}$ = 45ºC and 55ºC and $\dot{m}_{HTF}$ = 0.0026 kg/s.

Experiment	Avg. Melting Rate
45ºC Benchmark	3.8 ± 0.4 g/min
45ºC Heat pipe	6.4 ± 0.3 g/min
45ºC Fin	4.3 ± 0.1 g/min
55ºC Benchmark	6.6 ± 1.1 g/min
55ºC Heat pipe	11.5 ± 1.5 g/min

The thermal energy absorbed by the PCM consists of both sensible and latent components. The Stefan number for any of the $T_{HTF,in} = 45$ºC charging experiments may be expressed as

$$Ste_c = \frac{c_{p,s}\left(T_f - T_{i,c}\right) + c_{p,\ell}\left(T_{HTF,in} - T_f\right)}{\lambda} = 0.18 \tag{2.1}$$

Therefore, the sensible component is significant, and energy storage rates cannot be quantified based solely upon melting rates. Rather, energy storage in the PCM may be deduced by time-integrating the heat transfer from the HTF to the PCM expressed as

$$E_{t,c} = \sum_{i=1}^{n}[c_{p,HTF}\dot{m}_{HTF}\left(T^i_{HTF,in} - T^i_{HTF,out}\right)\Delta t - c_{p,HX}m_{HX}\left(T^i_{HX} - T^{i-1}_{HX}\right)] \tag{2.2}$$

where $E_{t,c}$ is the thermal energy stored in the PCM over time $t = i\Delta t$. The second term on the RHS of Eq. 2.2 is a correction to account for the thermal energy stored in the heat exchanger, heat pipe, and fin hardware. Because of the relatively small HTF flow rate, it was determined experimentally that $T_{HX} \approx T_{HTF,out}$, enabling use of the acquired thermocouple data to determine $E_{t,c}(t)$. The relation between T_{HX} and $T_{HTF,out}$ is discussed in Appendix 2.B. This calculation excludes the effect of heat exchange with the environment which is estimated to be approximately 15% (30%) of the total energy measured during the charging (discharging) experiments.

Figure 2.4a shows the energy stored in the PCM for the benchmark, heat pipe, and fin experiments. Three distinct melting regimes appear in all three cases. The first corresponds to a relatively rapid accumulation of energy in the PCM within the first 10 min of each experiment, when maximum temperature differences exist between the HTF

and the contents of the test cell. The second regime is associated with a nearly steady heat transfer rate to the PCM, as natural convection proceeds with a relatively time-invariant heat transfer coefficient between the solid surfaces and the solid-liquid interface(s), reflecting the proportionality for laminar natural convection $Nu_{H_l} \approx Ra_{H_l}^{1/3}$ (Bergman et al., 2011). A third regime corresponds to a sudden increase in the heat transfer rate due to close contact melting, such as shown in Fig. 2.2c for the heat pipe-assisted case. As expected, the charging rate is lowest (highest) for the benchmark (heat pipe-assisted) case. Similar experiments were conducted with $T_{HTF,in}$ = 55ºC and $\dot{m}_{HTF}$ = 0.0026 kg/s for both heat pipe and benchmark experiments. The three regimes evident in Fig. 2.4a are also noted in Fig. 2.4b and faster PCM melting occurs, as expected.

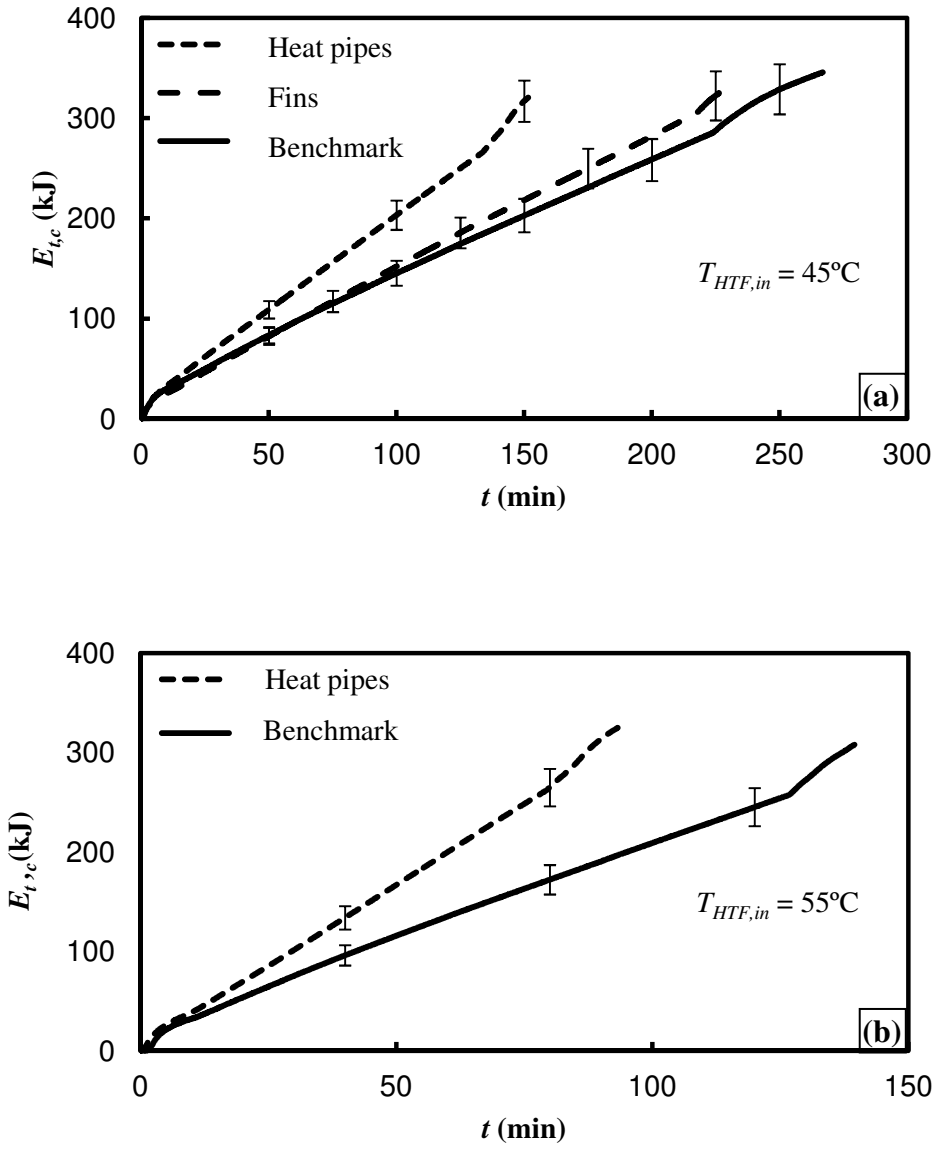

Figure 2.4: Energy stored in the PCM for the benchmark, heat pipe-assisted and fin-assisted cases. (a) $T_{HTF,\,in}$ = 45ºC and $\dot{m}_{HTF}$ = 0.0026 kg/s, (b) $T_{HTF,\,in}$ = 55ºC and $\dot{m}_{HTF}$ = 0.0026 kg/s.

To quantify the energy storage augmentation associated with use of heat pipes or fins, an effectiveness (Shabgard et al., 2010) may be defined as

$$\varepsilon_{HP,c} = \frac{E_{t,c,HP}}{E_{t,c,BM}} \quad ; \quad \varepsilon_{Fin,c} = \frac{E_{t,c,Fin}}{E_{t,c,BM}} \tag{2.3, 2.4}$$

where $E_{t,c,HP}$ ($E_{t,c,Fin}$) is the energy accumulated in the heat pipe (fin) configuration, and $E_{t,c,BM}$ is the energy accumulated in the benchmark case. The measured heat pipe effectiveness for $T_{HTF,in}$ = 45ºC is included in Fig. 2.5a. Initially, $\varepsilon_{HP,c}$ is large as conduction-dominated melting commences from the bottom plate and the heat pipes concurrently warm to the PCM melting temperature. Melting initiates at the heat exchanger surface in both the benchmark and heat pipe cases. Hence, the effectiveness initially decreases until secondary melting begins about the heat pipes. At *SteFo* = 0.001 (t = 5 min), a minimum $\varepsilon_{HP,c}$ is noted, after which the onset of melting about the periphery of the heat pipes ensues. The heat pipe effectiveness increases with time due to the strengthening of secondary and tertiary melting. The sharp increase in $\varepsilon_{HP,c}$ at *SteFo* = 0.025 (t = 130 min) is associated with close contact melting, as discussed relative to Fig. 2.2c.

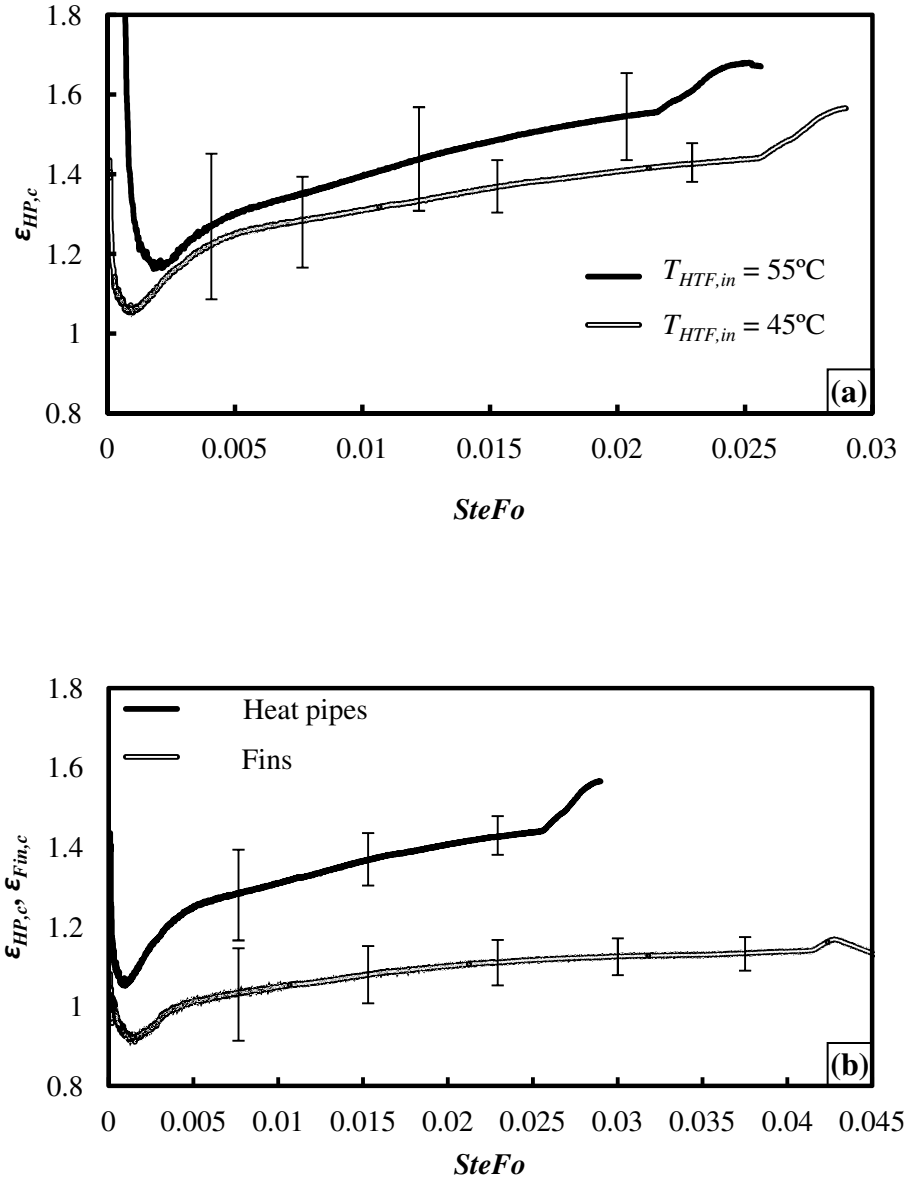

Figure 2.5: Effectiveness histories. (a) ε_{HP} for $T_{HTF,\,in}$ = 45ºC and 55ºC, and $\dot{m}_{HTF}$ = 0.0026 kg/s, (b) ε_{HP} and ε_{Fin} for $T_{HTF,\,in}$ = 45ºC and $\dot{m}_{HTF}$ = 0.0026 kg/s.

Figure 2.5a includes the $\varepsilon_{HP,c}$ history for the $T_{HTF,in}$ = 55ºC experiment. As evident, the higher HTF temperature case yields slightly higher effectiveness values, and the trends are similar to those noted for the lower HTF temperature experiment. The higher values are attributed to enhanced convection effects in the vicinity of the secondary and tertiary melt fronts that develop in the heat pipe experiments, and differences in heat losses with the environment relative to the lower temperature case. Notably, the experimentally-determined $\varepsilon_{HP,c}$ histories bear a remarkable similarity to those predicted for a large scale heat pipe-assisted LHTES system (Shabgard et al., 2010), with the exception of the close contact melting regime which was not included in the model of Shabgard et al. (2010).

The heat pipe and fin effectiveness histories are compared in Fig. 2.5b for the $T_{HTF,in}$ = 45ºC experiment. As evident, the fins are only marginally effective at augmenting energy storage rates. The impact of close contact melting is again evident during the last stages of the fin-assisted experiment.

2.4.2. Discharging Operation

Figure 2.6 includes photographs at intervals of Δt = 1 h for benchmark (left), heat pipe-assisted (middle), and fin-assisted (right) operation, with $T_{HTF,in}$ = 10ºC and $\dot{m}_{HTF}$ = 0.0022 kg/s. At t = 1 h, the benchmark experiments exhibit a planar solidification front adjacent to the top plate of the heat exchanger. Slight waviness (not evident in the photographs) was observed along the surface of the solidified PCM. The growth of the solidification front slowed with time in response to the increasing thermal resistance

posed by the solid layer. Average thicknesses of the solid PCM, measured to within ± 1 mm, are listed in Table 2.3.

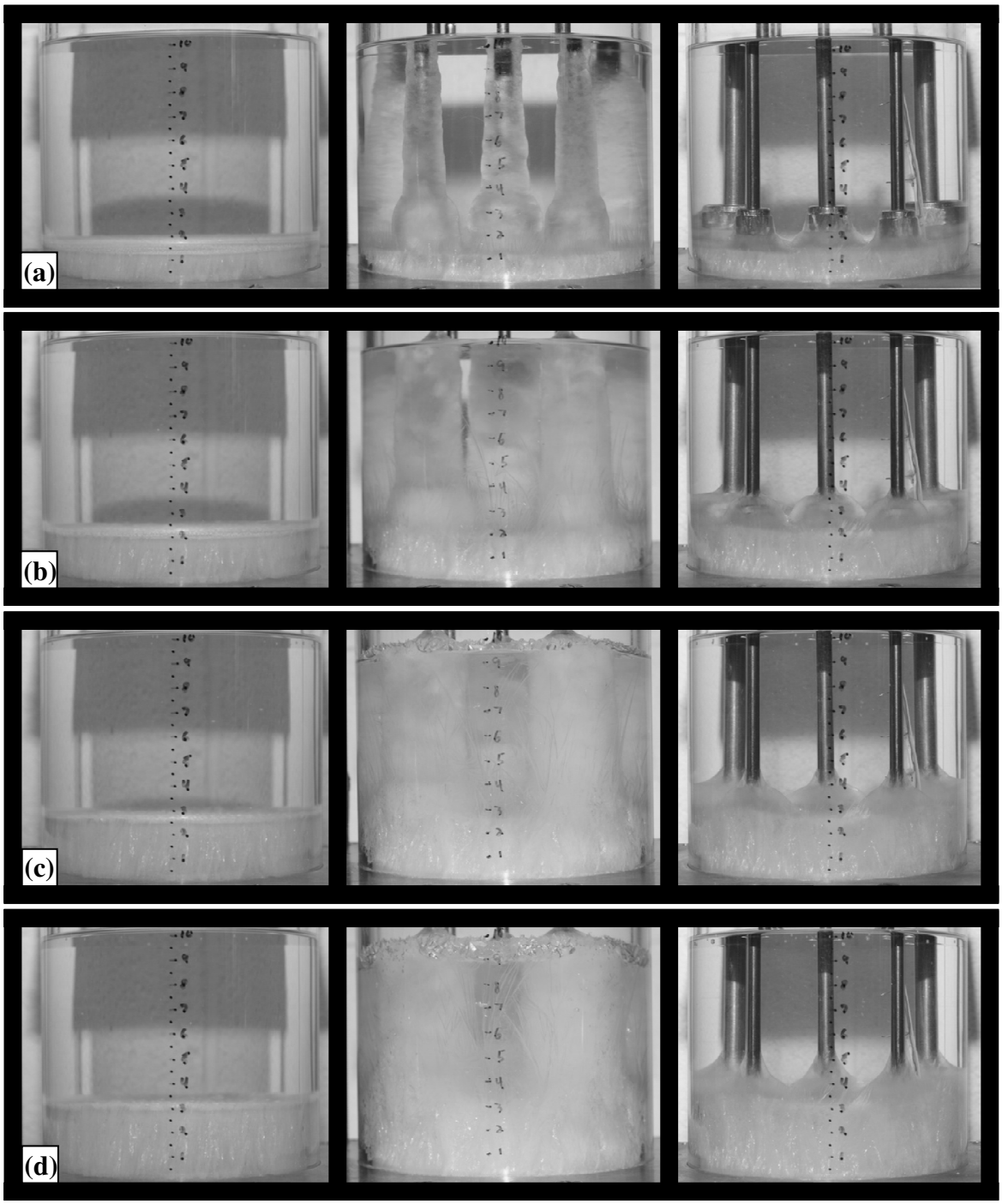

Figure 2.6: Temporal evolution of solidification for the benchmark (left), heat pipe-assisted (middle) and fin-assisted (right) cases. (a) t = 60 min, (b) t = 120 min, (c) t = 180 min, (d) t = 240 min ($T_{HTF,\,in}$ = 10ºC, $\dot{m}_{HTF}$ = 0.0022 kg/s, vertical scale in units of cm).

Table 2.3: Measured thickness of solid PCM on heat exchanger surface for benchmark experiments, and thickness of solid PCM around heat pipes for $T_{HTF,in}$ = 10ºC and $\dot{m}_{HTF}$ = 0.0022 kg/s.

t (min)	t_{BM} (mm)	t_{HP} (mm)
30	5	2.2
60	11	6.9
90	14	10.5
120	19	11.8
180	23	17.1
240	28	20.1

The heat pipe-assisted experiments (middle column of Fig. 2.6) reveal fundamentally different solidification phenomena relative to the benchmark case. Specifically, multiple solidification fronts form both along the top of the heat exchanger, and around the peripheries of heat pipes (as well as around the fittings holding the heat pipes in place). At t = 1 h, a 7 ± 2 mm thick layer of solid PCM forms around each heat pipe. The solid PCM layer is thinner near the top of the heat pipes due to the slight effects of thermal stratification in the liquid PCM. As time progresses, the solid PCM propagates outward from the heat pipes, and eventually fills most of the test cell (e.g. at Δt = 3 h).

As evident in Fig. 2.6, the fins provide little augmentation of the overall solidification rate, relative to the benchmark case. At t = 1 h, for example, only minor secondary freezing occurs in the vicinity of the fittings, with no solid PCM observed along the fin surface. At later times solid PCM forms about the fins, but upward propagation rates relative to the layer solidifying adjacent to the cooled upper surface of the heat exchanger are minor. At t = 4 h the mass of PCM solidified was 286 ± 15 g, 814 ± 15 g and 344 ± 15 g for the benchmark, heat pipe-assisted, and fin-assisted cases, respectively. Hence, the heat pipes (fins) led to a 180 % (21 %) increase in the time-averaged solidification rate. The mass of PCM that was solidified along with the corresponding latent energy content of the solidified PCM, $E_{LH,dc}$, for the three cases of Fig. 2.6 is shown in Fig. 2.7.

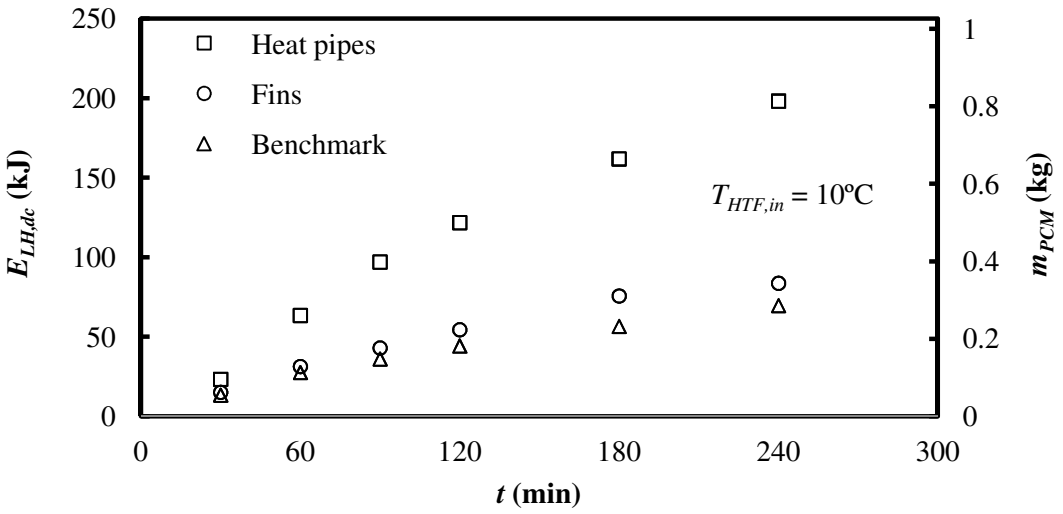

Figure 2.7: Mass of solid PCM and latent energy released for the benchmark, heat pipe-assisted, and fin-assisted discharging experiments. Error bars are not shown since the error is relatively small.

The Stefan number for the discharging experiments may be expressed as

$$Ste_{dc} = \frac{c_{p,\ell}(T_i - T_f) + c_{p,s}(T_f - T_{HTF,in})}{\lambda} = 0.27 \tag{2.5}$$

As in the charging experiments, the sensible energy content of the PCM represents a significant portion of its energy budget. Energy discharged from the PCM may be estimated using

$$E_{t,dc} = \sum_{i=1}^{n} [c_{p,HTF}\dot{m}_{HTF}(T^i_{HTF,out} - T^i_{HTF,in})\Delta t + c_{p,HX}m_{HX}(T^i_{HX} - T^{i-1}_{HX})] \tag{2.6}$$

The discharged energy is shown in Fig. 2.8a for the benchmark, heat pipe-assisted, and fin-assisted experiments. Because the process is, in large part, conduction-dominated the heat transfer rates diminish with time. The heat released from the PCM was largest for the heat pipe-assisted case, while the fin-assisted case was found to perform only slightly better than the benchmark. These results are expected, given the photographic observations of Fig. 2.6, and solidification histories of Fig. 2.7.

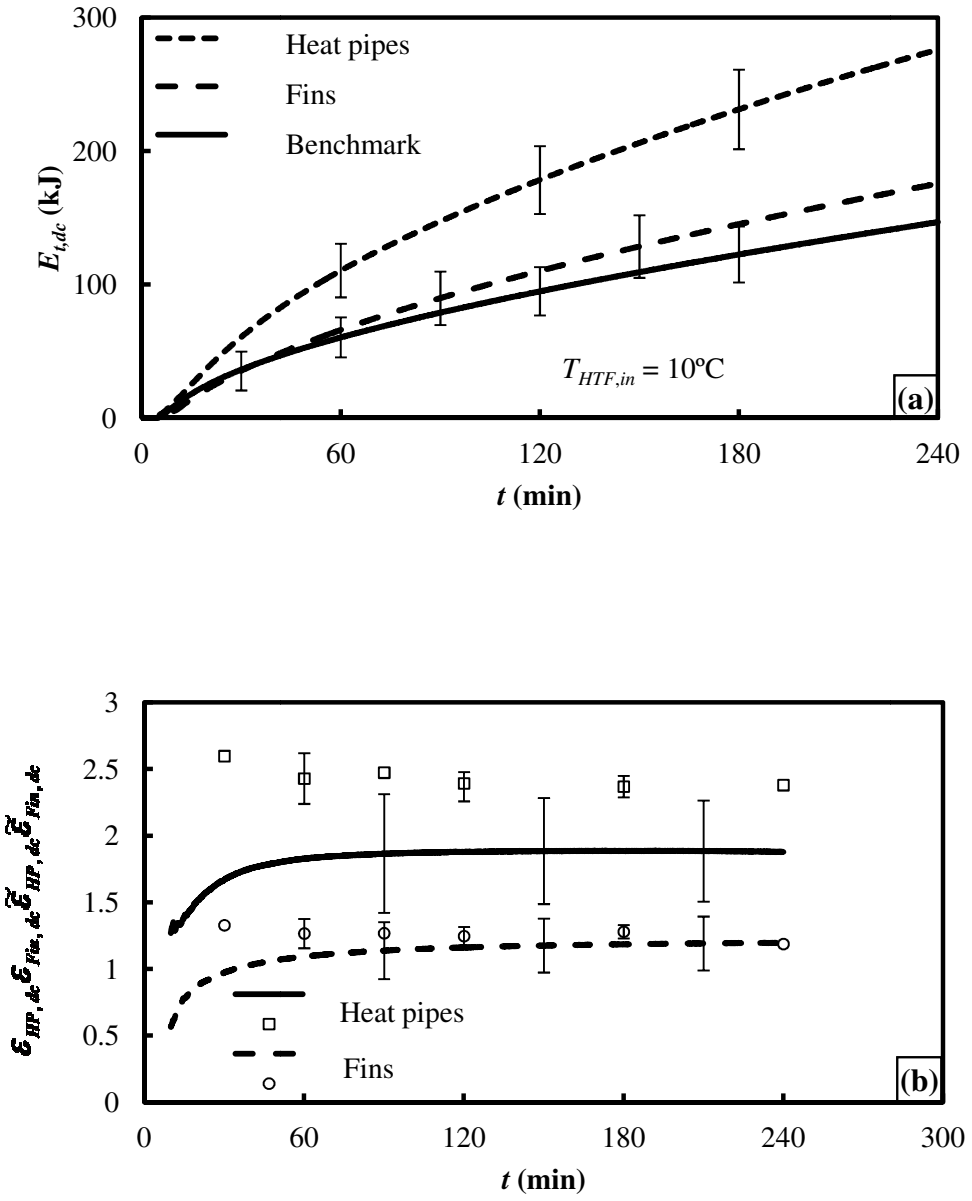

Figure 2.8: (a) Energy released from PCM for the benchmark, heat pipe-assisted, and fin-assisted experiments from Eq. 2.6 ($T_{\mathrm{HTF,\,in}}$ = 10ºC, $\dot{m}_{\mathrm{HTF}}$ = 0.0022 kg/s). (b) Heat pipe and fin effectiveness, using Eqs. 2.6 (lines) and 2.7 (symbols).

Heat pipe and fin effectiveness values for discharging ($\varepsilon_{HP,dc}$ and $\varepsilon_{Fin,dc}$) were calculated in the same manner as in Eq. 2.3, and are presented in Fig. 2.8b. These histories appear as solid lines. Because of the large uncertainty during the first 10 min of the experiments, early values of the effectiveness are not shown. At $t \approx 10$ min, $\varepsilon_{HP,dc}$ exceeds unity and gradually reaches an asymptotic value of approximately 1.9, where it remains for the duration of the experiment. The fin effectiveness exhibits a similar trend. However, it reaches a maximum value of only 1.1.

The evolution of the energy content of the PCM may also be estimated using information from the thermocouple rake. Specifically,

$$\tilde{E}_{t,dc} = m_{PCM,s}\lambda + m_{PCM,s}c_{p,s}\left(\frac{T_f - T_{HX}}{2}\right) + m_{PCM,s}c_{p,s}\left(T_i - T_f\right) + m_{PCM,\ell}c_{p,\ell}\left(T_i - T_{PCM,\ell}\right) \quad (2.7)$$

where the first term on the RHS of Eq. 2.7 represents the energy released in the form of latent heat, calculated from the mass of frozen PCM reported in Fig. 2.7a. The second term on the RHS represents the average energy content of the solid, assuming a linear temperature distribution within the solid phase. The third term represents the reduction in energy content of liquid prior to its solidification and the last term corresponds to sensible energy associated with reduction of the liquid from its initial warm temperature, T_i. The thermocouple rake data were used to estimate the liquid phase PCM temperature at any time, $T_{PCM,\ell}$. The estimated uncertainty in $\tilde{E}_{t,dc}$ is ± 2- 20%. Values of $\tilde{\varepsilon}_{HP,dc}$ and $\tilde{\varepsilon}_{Fin,dc}$ are presented as data points in Fig. 2.8b. Using the modified method to calculate the heat pipe effectiveness yields higher values relative to use of Eq. 2.6. However, the effectiveness data obtained by reducing experimental measurements with the two

methods are generally consistent within the estimated experimental uncertainty. Fin effectiveness values, calculated with the two approaches, are in good agreement and exhibit the limited effectiveness of the fins.

2.5. Experimental Conclusions

Charging (melting) experiments have yielded photographic evidence showing more extensive and complex melting phenomena for heat pipe-assisted melting, relative to both benchmark and fin-assisted cases. The overall melting rates for the heat pipe-assisted cases were, on average, 70% greater than the benchmark and 50% greater than the fin-assisted scenario. The heat pipe effectiveness, defined as the ratio of stored energy in the heat pipe-assisted case relative to stored energy in the benchmark case, attained at a maximum value of 1.6, while the maximum effectiveness associated with use of fins was approximately 1.1.

For the discharging (solidification) case, complex freezing phenomena were observed for the heat pipe-assisted scenario. The heat pipes nearly doubled the solidification rates, relative to the benchmark case. The fins exhibited limited effectiveness in enhancing heat transfer and energy storage rates.

The experiments conducted and analyzed do not correspond to optimized conditions. Further investigation is necessary to determine how heat pipes might be incorporated in LHTES systems to improve phase change rates beyond those measured here, reduce temperature differences between the HTF and PCM (which has a direct and beneficial impact on the Rankine cycle efficiency of concentrating solar thermal electric power stations), and occupy minimal volume within the LHTES storage vessel. The

observed phenomena and measured values can be used to guide model development for purposes of simulating the discharging and charging processes in both laboratory- and large scale systems.

2.6. Appendix 2.A

For any LHTES application, fins of high efficiency or effectiveness are desirable. Regardless of the fin material, the fin efficiency will increase as the physical dimensions (thermal conductivity) of the fin become small (large); heat pipe performance is not as sensitive to the size of the device. Therefore, to mimic the efficiency of a large fin in a laboratory scale experiment, a smaller fin with a lower thermal conductivity relative to that of the larger fin is needed so that $\eta_{Fin,LS} \approx \eta_{Fin,SS}$.

Assuming free convection heat transfer occurs within relatively thin boundary layers about vertical fins of length L in a manner that can be described as $Nu_{L_{Fin}} = CRa_{L_{Fin}}^{n}$, $C \approx 0.59$, $n = 1/3$ ($C \approx 0.10$, $n = 1/4$) for laminar (turbulent) conditions (Bergman et al., 2011). Also assuming (*i*) fluid properties similar to those of n-octadecane, (*ii*) the same characteristic temperature difference in both the large and small scale systems, (*iii*) the same fin length-to-diameter ratio in both systems, and (*iv*) a large scale fin length of $L = 1$ m, it may be shown that if aluminum, $k \approx 250$ W/m·K, is used as the fin material in the large scale system, $k_{SS} \approx 33.5$ W/m·K. Therefore, stainless steel was specified as the fin material for the small scale experiments of this study.

2.7. Appendix 2.B

Heat exchanger and HTF outlet temperature histories are shown in Fig. 2.9 for a $T_{HTF,in}$ = 45°C charging experiment. As evident, $T_{HX} \approx T_{HTF,out,}$ for the entire duration of the test. The heat exchanger temperature was measured with five calibrated K-type thermocouples that were installed using high thermal conductivity paste in equally-spaced, 10-mm deep holes bored into the bottom of the aluminum heat exchanger along the horizontal centerline in Fig 2.1b. The approximation used in Eqs. 2.2 and 2.6 were utilized since the initial charging experiments were conducted without direct measurement of the heat exchanger temperature.

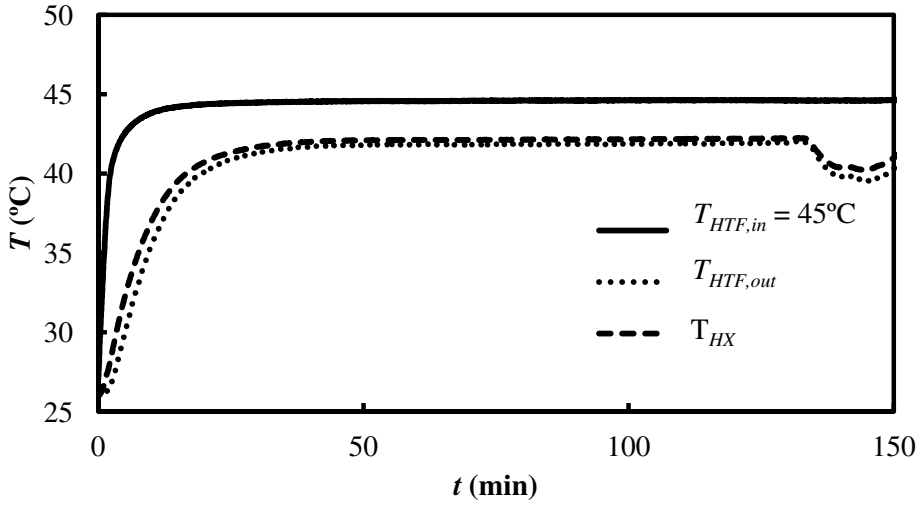

Figure 2.9: HTF inlet, HTF outlet, and heat exchanger temperatures for charging heat pipe-assisted experiment ($T_{HTF,\,in}$ = 45ºC and $\dot{m}_{HTF}$ = 0.0022 kg/s). Error bars are not shown since the error is relatively small.

Chapter 3. LHTES Modeling and Economic Analysis

3.1. Motivation

With the experimental results as a proof of concept that heat pipes can reduce the thermal resistance in PCM, the third chapter of this thesis will investigate a conceptual commercial scale LHTES design. Specifically, the incorporation of gravity-assisted wickless heat pipes (thermosyphons) in a large scale LHTES system for commercial CSP is of interest. A LHTES system design is proposed which can operate effectively during a charging and discharging period. A heat transfer model is utilized to estimate, for example, the size and number of thermosyphons needed in the LHTES. An economic evaluation of the system is carried out, and the design is compared with a two-tank SHTES to determine whether LHTES with embedded thermosyphons can be cost-competitive (Robak et al., 2011b).

3.2. LHTES Integration with CSP

A LHTES system capable of releasing sufficient thermal energy to continually operate a 50 MW_e CSP plant with discharging (PCM solidification) times varying from 1 to 9 hours is considered here. Both experimental (Robak et al., 2011a) and analytical (Shabgard et al., 2010) studies have shown that the thermal resistance posed by the PCM is greater during the discharging stage (PCM solidification) than during charging. This is because solid, low thermal conductivity PCM freezes on cold heat transfer surfaces during PCM solidification, in effect forming an insulation barrier between the HTF and the solid-liquid interface of the PCM. In contrast, molten PCM that undergoes natural convection is adjacent to hot heat transfer surfaces during PCM melting, promoting heat transfer between the hot HTF surface and the solid-liquid interface of the PCM. As such,

the discharging process is of primary concern; any design that performs well during discharging is expected to operate satisfactorily during charging.

Figure 3.1 is a schematic of a CSP plant equipped with LHTES operating in the discharging mode. During discharging, the HTF flow from the solar field is curtailed, and the HTF is pumped only through the LHTES unit. The PCM within the LHTES solidifies, and releases thermal energy to the HTF. The PCM-heated HTF is sent to the steam generator, keeping the plant operational during times of low- or no solar insolation. The overall design is similar to a two-tank SHTES system; however, LHTES does not require extra salt pumps as does SHTES, reducing both the capital cost and the parasitic pumping losses during the charging and discharging processes. The salt pumps also consume electrical power, which incurs an extra operating cost which the proposed LHTES will not have. During charging (not shown) the HTF flows though the solar field, where it is warmed through a system of parabolic trough mirrors that concentrate the solar irradiation. Part of the hot HTF flows into the steam generator while the remaining hot HTF is diverted to the LHTES storage unit, where it melts the PCM, storing thermal energy. The two HTF streams are re-combined and pumped back to the solar field to be reheated.

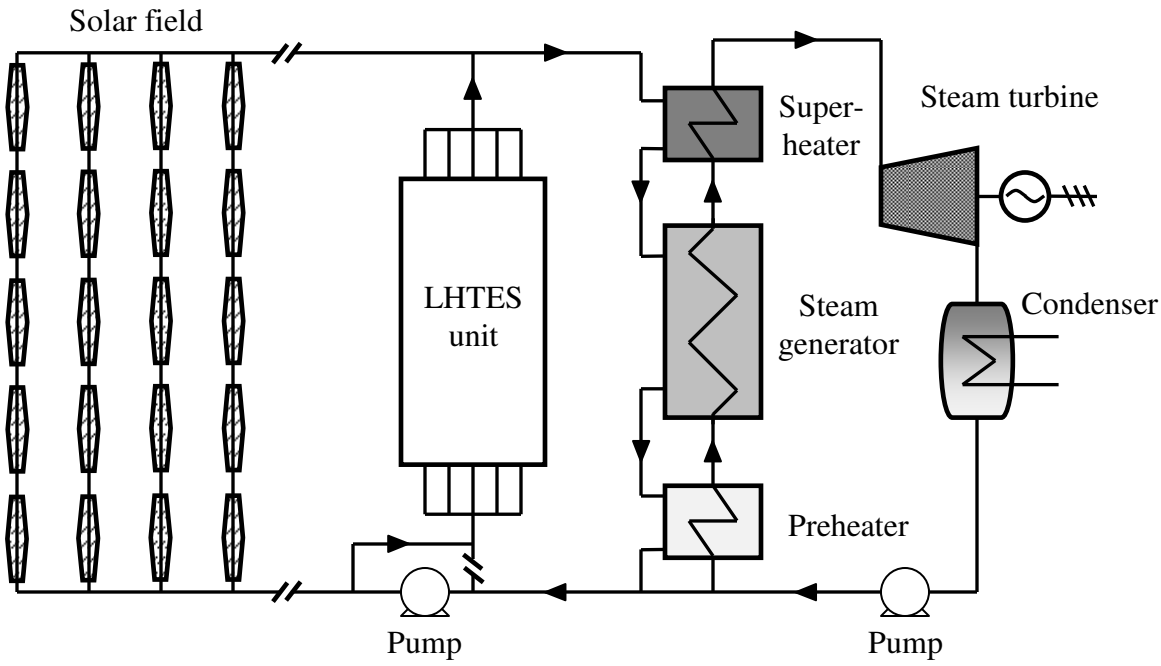

Figure 3.1: LHTES system integrated with a CSP plant.

3.3. LHTES with Embedded Thermosyphons: Conceptual Design

The LHTES unit of Fig. 3.1 must be carefully designed to promote effective heat transfer between the HTF and the solidifying PCM. In particular, a means to circumvent the undesirable effect of solid PCM growth on cold heat transfer surfaces during LHTES discharging is of primary concern. An additional design constraint is that variations in the steam conditions and flow rates delivered to the CSP power block are kept within an acceptably small range during LHTES operation. The outlet temperature of the HTF from the solar field is assumed to be 390°C (Herrmann et al., 2004).

The design considered here incorporates thermosyphons (Faghri, 1995) to promote heat transfer between the cold HTF and the solid-liquid interface of the hot PCM. As shown in Fig. 3.2, the LHTES unit might consist of a header (not shown) that partitions the cold HTF into a series of channels within the LHTES unit. Each HTF channel is studded with an array of thermosyphons that span between the HTF and PCM. As such, the HTF channels, along with the thermosyphons, are the surfaces upon which the PCM solidifies. For a given amount of solid PCM, (a) the surface area of the PCM's solid-liquid interface is large compared to the case without thermosyphons, and (b) the mean distance between the cold surfaces and the PCM solid-liquid interface is small, compared to the case without thermosyphons. These dual effects ─ increased solid-liquid interface area and reduced distances between the solid-liquid interface and the cold HTF surface ─ will reduce the thermal resistance between the cold HTF and the solidifying PCM. At the LHTES unit exit, a second header (not shown) combines the individual heated HTF streams. During charging, the direction of HTF flow through the LHTES unit is reversed and the HTF is cooled as it melts the PCM. To reiterate, natural

convection occurs within the molten PCM that is adjacent to the hot surfaces during LHTES charging, resulting in a low thermal resistance between the HTF and the PCM's solid-liquid interface relative to the conduction-dominated discharging process.

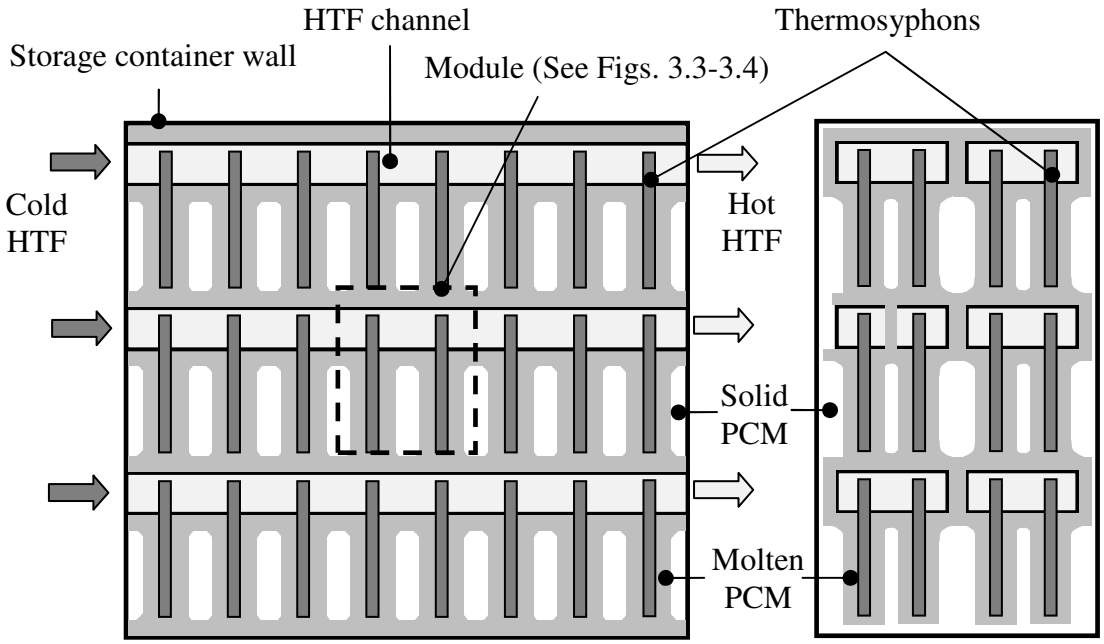

Figure 3.2: Cross-sectional views of a LHTES system with embedded thermosyphons during discharging. (a) Lengthwise view and (b) widthwise view. The dashed box corresponds to a unit module.

Thermosyphons are considered here (instead of heat pipes) because of their simplicity of construction and operation, as well as their lower cost (Faghri, 1995). Also, for reasons discussed in Section 3.5.2.1, thermosyphons are preferred over extended surfaces or fins. Since thermosyphons operate only when the direction of heat transfer is opposite that of gravity, the evaporator sections of the thermosyphons must be at the lower end of the devices. However, it is desirable that the integration of thermosyphons into the LHTES unit be done in a unique manner that allows operation during both the discharging and charging cycles.

For thermosyphons to assist in heat transfer regardless of the mode of operation (discharging or charging), they are assumed to penetrate the bottom wall of each HTF channel, as shown in Fig. 3.2. By carefully positioning the thermosyphons, they only need to be implanted into one HTF channel, reducing fabrication costs. The thermosyphons might be either press fit or inertia welded into the HTF channel wall before shipment to the construction site (Miner et al., 2010). Because the direction of heat transfer is upward during LHTES discharging, the configuration of Fig. 3.2 is expected to work well during PCM solidification.

3.3.0.1 Discharging

During the discharging process, thermal energy is released from the PCM to the HTF through two different paths, as shown in Fig 3.3a. Latent heat from within the PCM is transported into the HTF with the embedded thermosyphons, causing solidification fronts to expand out from the surface of the thermosyphons. Additional thermal energy is conducted through the channel wall, causing a second solidification front to expand into

the molten PCM. The arrows in Fig 3a show the direction of heat flow during the discharging process. Given enough thermosyphons, all of the PCM between two adjacent HTF channels is solidified by the end of the discharging operation.

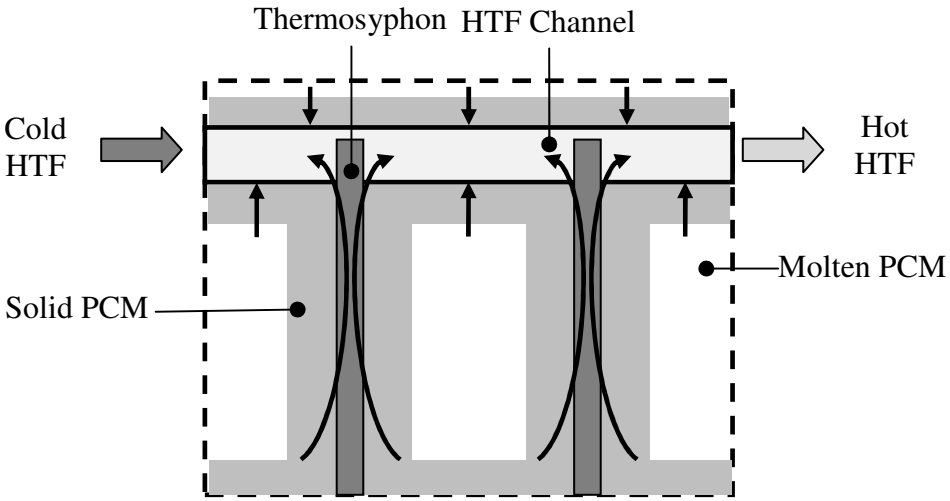

a) LHTES discharging

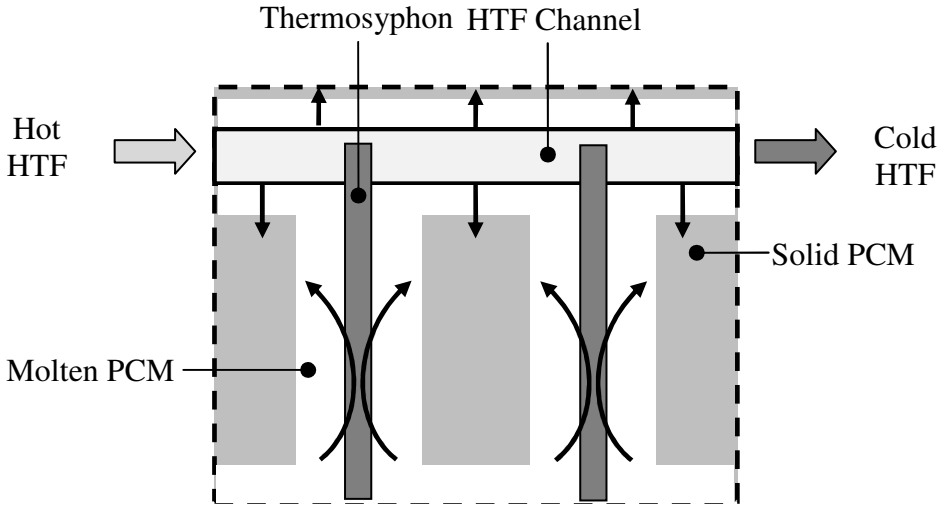

b) LHTES charging

Figure 3.3: Side view of LHTES heat transfer paths. (a) Discharging and (b) charging. The arrows represent the direction of heat transfer.

3.3.0.2 Charging

During the charging operation, the direction of heat flow relative to the solid PCM is reversed from discharging, as shown by the arrows in Fig. 3.3b. Like discharging, heat is transferred through the HTF channels walls and thermosyphons during charging. Since the evaporator ends of the thermosyphon are not exposed to the hot HTF during charging, heat is primarily transferred through the HTF channel wall early in the charging process. Once the melting front moving out from the lower HTF channel wall reaches the ends of the thermosyphons, they begin to operate, transferring thermal energy deeper into the PCM. Additionally, during the charging operation, thermosyphons create many fluid passages, which enhance natural convection currents and allows expanding molten PCM to flow towards internal voids, minimizing pressure forces in the LHTES unit (Robak et al., 2011).

3.3.1 Detailed Design

Details of the conceptual design are considered now. First, the PCM will be specified, then the design of the thermosyphons will be presented, followed by a discussion of the integration of the LHTES with the steam generator. A model will then be presented that is used to quantify performance, and estimate costs.

3.3.1.1 PCM Selection

Candidate PCMs are listed in Table 3.1. Materials with melting temperatures less than approximately 340ºC result in a relatively low temperature HTF leaving the LHTES during discharging, which adversely affects the thermodynamic efficiency of the power (Rankine) cycle. Alternatively, PCMs with a relatively high melting temperature, such as

the $MgCl_2$/KCl/NaCl mixture, may lead to reduced heat transfer rates between the HTF and the PCM during charging because of the relatively small temperature difference between the two media (Michels and Pitz-Paal, 2007). Therefore, a mixture of LiCl/KCl is selected for this study because its melting temperature (348°C) is approximately midway between the 280ºC LHTES HTF inlet temperature specified for modern CSP operation during discharging, and the 390°C HTF coming from the solar field during charging (Kelly and Kearney, 2006).

Table 3.1: LHTES PCM candidates

PCM (Wt. %)	Melting Point (ºC) (Kenisarin, 2010)	Heat of Fusion (kJ/kg) (Kenisarin, 2010)	EstimatedCost (US$/kg)*
$NaNO_3$	307	177	0.41
$NaOH/NaCl/Na_2CO_3$ (65.2/20.0/14.8)	318	290	0.31
KNO_3	335	88	0.62
LiCl/KCl (44.0/56.0)	348	170	0.50
KOH	360 (Faghri, 1995)	134 (Faghri, 1995)	1.00
$MgCl_2/KCl/NaCl$ (60.0/20.4/19.6)	380	400	0.46

*Estimates derived from Kensisarin, 2010, and general internet searches for bulk priced materials (Alibaba.com, 2011).

3.3.1.2 Thermosyphon design

The thermosyphons are assumed to be fabricated of carbon steel to minimize the potentially adverse effects of corrosion at the thermosyphon-channel (carbon steel) interface. The thermosyphon working fluid must be capable of operating between approximately 300ºC and 400ºC, and it is assumed each thermosyphon is filled to 10% of its internal volume with the working fluid. Therminol VP-1, diphenyl, naphthalene, and potassium were considered as candidate thermosyphon working fluids. The length and diameter of the thermosyphons are dependent on the particular LHTES application. As will be explained later, thermosyphons with a total length of L_{TS} = 0.58 m, and diameter, D_{TS} = 0.024 m, with Therminol VP-1 as the working fluid were selected. Currently, the same fluid is used as the HTF in CSP applications, suggesting its material compatibility and long-term stability.

3.3.1.3 Steam Generation System

The thermodynamic efficiency of the power block is largely determined by the conditions exiting the steam generator. Modern CSP plants are designed to operate (with HTF routed directly from the parabolic collectors during the day) at a steam inlet temperature and pressure of approximately 380ºC and 100 bars, respectively (Kelly and Kearney, 2006). When TES is implemented, the system utilizes the same steam generation heat exchangers as for daytime operation, as shown in Fig. 3.1. Since the overall heat transfer area of the steam generator is determined based upon daytime operation, the reduction in HTF temperature during TES operation leads to lower heat transfer rates and, in turn, generation of less steam at lower temperature. To

counterbalance this effect, the steam pressure is reduced when the TES is used (Miner et al., 2010). By lowering the steam pressure, the water saturation temperature is reduced, increasing the temperature difference between the HTF and the steam, increasing heat transfer and steam generation rates. This effect will be accounted for when estimating the Rankine cycle efficiency and its dependence on the type of TES system utilized.

The ideal Rankine cycle efficiency for different CSP operations can be calculated with general thermodynamic relations (Moran and Shapiro, 2011). Table 3.2 provides the Rankine cycle efficiency expected for steam generated from (a) HTF taken directly from the solar field during daytime operation, (b) HTF exiting a SHTES unit, and (c) HTF exiting the LHTES proposed here. To calculate the steam pressures and Rankine cycle efficiencies of Table 3.2, a simple heat exchanger analysis is conducted, utilizing the following assumptions:

- The power output of the plant is constant and equal to 50 MW_e.
- The steam generation system is comprised of three separate heat exchangers, a water preheater, a steam generator, and a superheater, operating in counter flow as shown in Fig. 3.1.
- The heat exchange areas of the preheater, generator and superheater are calculated based upon daytime operation and steam outlet conditions of 380ºC and 100 bar, and it is assumed that nighttime operation at lower pressure corresponds to a higher steam flow rate.
- Overall heat transfer coefficients in the heat exchangers are assumed to be 1,000 $W/m^2 \cdot K$ (Kelly and Kearney, 2006).

- Steam outlet temperatures are assumed to be 10ºC lower than the HTF inlet temperature (Kelly and Kearney, 2006).
- The HTF temperature exiting the proposed LHTES unit is assumed to be 340ºC.
- The HTF temperature at the outlet to the heat exchanger is assumed to always be 280ºC, matching the HTF temperature entering the solar field (Kelly and Kearney, 2006).
- The outlet pressure of the steam turbine is assumed to be 0.1 bar.

Table 3.2: Expected ideal Rankine cycle efficiencies for different HTF sources

HTF Source	Temperature HTF (ºC)	Temperature Steam (ºC)	Pressure Steam (Bar)	Rankine Cycle Efficiency
Solar Field	390	380	100	0.385
SHTES	370	360	78	0.373
Proposed LHTES	340	330	50	0.353

In the analysis, the heat exchange area of the steam generation system for daytime operation is initially calculated. Then, the HTF temperature is set to either 370°C or 340°C to consider night operation with a SHTES or LHTES, respectively. Once this is done, the high steam pressure of the Rankine cycle is reduced from the daytime value until the required area of the steam generator heat exchange surface matches the area initially calculated. After the reduced value of the high pressure of the Rankine cycle is known, the Rankine cycle efficiency is calculated. As the HTF temperature is reduced from 390ºC to 370ºC with SHTES, the high pressure of the Rankine cycle falls from 100 to 78 bars while the ideal Rankine cycle efficiency decreases from 0.385 to 0.373, matching previous SHTES calculations (Kelly and Kearney, 2006). For the proposed LHTES, the calculated steam pressure is 50 bars and the Rankine cycle efficiency is determined to be 0.353. Once the Rankine cycle efficiency is known, the required size and features of the LHTES unit may be found.

3.4. LHTES Modeling

To determine the size of an LHTES unit required to generate 50 MW_e at night, an existing model (Shabgard et al., 2010) was modified to simulate the discharging process. Again, only discharging is considered in the design, since charging generally involves lower thermal resistances between the HTF and the PCM. Hence the charging period is less than this discharging period. Specified parameters for the LHTES unit are the inlet and outlet HTF temperatures and HTF properties, the PCM properties, and the ideal Rankine cycle efficiency corresponding to the HTF flow conditions. Other conditions are input and their values are changed in a parametric study that is described in more detail later. Varied parameters include (for a specified electric power output) the width and

height of the HTF channels, the HTF channel wall thickness, the HTF mass flow rate per channel, the dimensions of the thermosyphons (outside diameter, wall thickness, overall length, and evaporator section length), and the desired operational time of the storage system. Based upon the input conditions and parameters, the model determines the overall length, width and height of the LHTES unit, the number and length of the HTF channels, and the number of thermosyphons needed. Heat transfer to or from the PCM includes both the sensible and latent energy storage quantities. Generally, the sensible energy component of the PCM storage is approximately 5% of the total energy stored.

Shabgard's thermal network model for LHTES with embedded heat pipes (Shabgard et al., 2010) was modified and used here. The LHTES system shown Figs. 3.2 and 3.3 is composed of a number of unit cells, or modules, such as the one shown by the dashed lines in Fig. 3.2. A representative module consists of two staggered rows of thermosyphons (into the page) and surrounding PCM, and is centrally-located in the LHTES unit. It is assumed that this module experiences HTF thermal conditions that are the average of the inlet and outlet temperatures, which are specified. The PCM is initially assumed to be liquid at its solidification temperature. Figure 3.4 provides a more detailed cross-sectional view of the LHTES module. The thermosyphons are arranged in staggered rows to minimize the thermal resistance associated with forced convection heat transfer between the HTF and the condenser section of the thermosyphon (Shabgard et al., 2010).

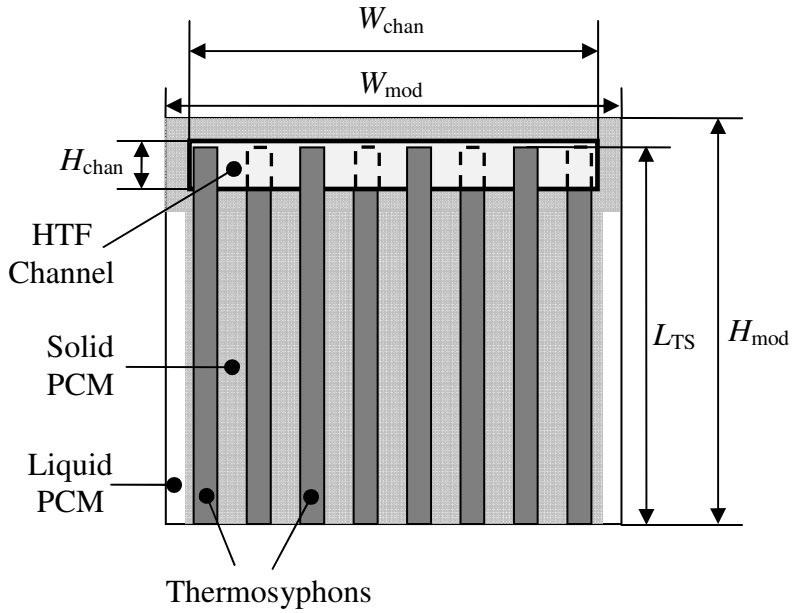

(a) Module Side View

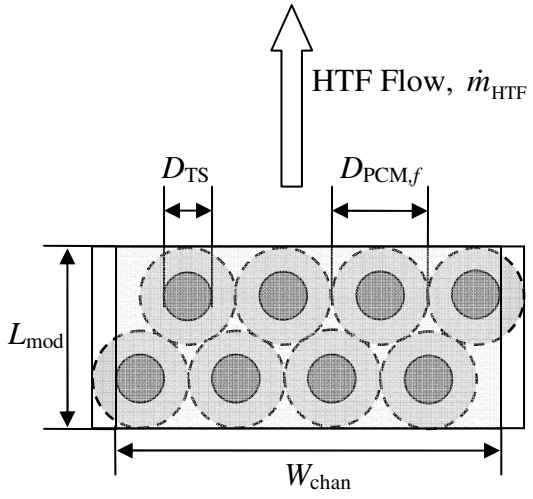

(b) Module Top View

Figure 3.4: Unit module, (a) side view and (b) top view.

The network model (Shabgard et al., 2010) is used to determine the heat transfer from the solidifying PCM to the HTF. Included in this calculation (for which potential contact resistances at the solid PCM-metal interfaces are neglected since the main resistance to heat transfer is associated with the low thermal conductivity of the solid PCM) is the time variation of the radius of solid PCM that forms on the condenser sections of the thermosyphons. The network model simulation is curtailed at the specified discharging period. Once the final radius of solid PCM, $D_{PCM,f}$, is determined, the number of thermosyphons that can be placed in the two staggered rows of the HTF channel (of specified width W_{chan}) is found using simple geometric arguments based upon Fig. 3.4b. The length (in the direction of HTF flow) of the module, L_{mod}, can be computed in a similar manner.

In addition to PCM solidification on the thermosyphon condenser sections, the network model computes the thickness of solid PCM that freezes on the four cold HTF channel surfaces. The module width, W_{mod}, is determined based upon the specified channel width, W_{chan}, plus twice the thickness of solid PCM around the sides of the HTF channels. The module height, H_{mod}, is found by adding the thickness of PCM along the top of the HTF channel with thermosyphon overall length, and HTF channel wall thickness. With the module width, length, and height determined, the overall size of the LHTES system can be computed as follows.

The total length (in the direction of the HTF flow) of each HTF channel is based upon the heat transferred in one module to the HTF from the solid PCM over the discharging period. Thus, with the mass flow rate of the HTF per module (or channel) specified, along with the HTF properties, the increase of the HTF temperature through a

single module can be computed. The number of modules (in the direction of the HTF flow) is then calculated based upon the temperature increase per module and the overall temperature increase over the entire LHTES. Hence, the total length of the LHTES can then be determined. Subsequently, the total number of HTF channels required is determined by calculating the thermal energy storage required of the LHTES unit, based on the specified electric power production of the Rankine cycle, and the efficiency that was determined and reported in Table 3.2. Finally, (a) the total size of the LHTES unit is found from knowledge of the total number of HTF channels and (b) the required number of thermosyphons is found from the total number of modules, the module size, the thermosyphon dimensions, and the thickness of the PCM solidified on the thermosyphons over the discharging period.

3.4.1. Cost Calculations

Once the physical details of the LHTES design are determined, the capital costs of the major components can be estimated based upon their size and mass. Capital costs for the LHTES unit are associated with four main system components: (1) the exterior storage container, (2) the PCM, (3) the thermosyphons, and (4) the internal architecture of the LHTES unit such as the HTF channels. Manufacturing and assembly cost estimates are included in the analysis and are based upon publically-available information (for example, Herrmann et al., 2004; Kelly and Kearney, 2006). In addition to the costs of the 4 major system components, a 10% overhead is added to the total capital cost. This overhead covers secondary components such as instrumentation, wiring, piping, valves, and insulation, and matches the rate used in a two-tank SHTES economic analysis (Herrmann et al., 2004). Specifics regarding the main system components follow.

3.4.1.1. LHTES Storage Container Cost

As noted previously, the length of a HTF channel is determined by the thermal network model. If the storage container height is specified, the width of the storage unit can be determined. Ultimately, the desired height and width of the storage container is associated with a low overall cost. To calculate the overall cost of the storage container, several assumptions are made. First, the shell of the storage container is assumed to be constructed of carbon steel, with an average wall thickness of 38 mm, which is consistent with values used in two-tank SHTES designs (Herrmann et al., 2004; Kelly and Kearney, 2006). Second, the assembly cost of the storage tank is based on the weight of the carbon steel needed for its construction. To be consistent with a previous SHTES analysis, the cost of materials and construction of the storage container is set at \$4.40/kg of carbon steel (Kelly and Kearney, 2006). In addition, the storage container foundation is assumed to be of the same construction as modern SHTES units, priced at \$688/m^2 (Kelly and Kearney, 2006). Also, calcium silicate insulation (\$200/m^2) is assumed to cover the outside of the storage container, with an average thickness of 380 mm (Kelly and Kearney, 2006).

3.4.1.2. PCM Cost

The mass of the LiCl/KCl PCM is calculated from knowledge of the empty volume of the PCM storage container, which is found by subtracting the volume of the heat transfer equipment within the container from its overall volume. The liquid density of the PCM is used to calculate the required mass (to account for expansion during

melting). The unit cost of the PCM is not well-established and is subject to change. As such, a range of unit costs will be considered in Section 3.5.

3.4.1.3. Thermosyphon Cost

The thermosyphons consist of a metallic shell and an internal working fluid. The overall length and diameter of the thermosyphons are treated as variables, and the impact of these dimensions on the overall cost is discussed in the *preliminary cost analysis* of Section 3.5.1. It is assumed that the thermosyphons have a 2-mm-thick carbon steel shell. The Therminol VP-1 working fluid is priced at $2.10/kg. A stainless steel screen wick is included to reduce resistance within the film of working fluid along the inner wall of the thermosyphon. As noted previously, the thermosyphons are fixed in the HTF channel wall using either a press fit or an inertia weld (Miner et al., 2010). In addition, the ends of the thermosyphons are welded shut, at a cost of $5.84/m (SSAB, 2010). The overall cost of each thermosyphon therefore varies with its length, diameter, and the bulk price of carbon steel. Note that in the *sensitivity analysis* of Section 3.5.2, the thermosyphon cost is de-coupled from the material costs for simplicity.

3.4.1.4. HTF Channel Cost

The carbon steel HTF channels are included in the overall LHTES system capital cost. The price of carbon steel used in this study is explained further in Section 3.5. The HTF channels walls are assumed to be 10 mm thick, and the weight of the HTF channels is calculated based upon their dimensions and the density of carbon steel. It is assumed that the channels would be delivered in 12 m long sections, which need to be welded during their assembly at an estimated cost of $20.45/m (SSAB, 2010).

3.4.1.5. SHTES Cost

To compare the SHTES and LHTES systems, the primary contributors to the capital cost of the SHTES also need to be identified. These are the solar salt, the molten salt heat exchanger and pumps, and the two storage containers and are taken primarily from Herrmann et al. (2004), who attributed roughly half of the total cost for SHTES to the inventory of solar salt needed.

3.5. Results and Discussion

As will become evident, an economic comparison between the SHTES and LHTES systems is subject to variability in the costs of the major components. Therefore, to compare SHTES to LHTES, ranges of different unit prices (in U.S. dollars) for each of the major components (excluding the storage containers for SHTES and LHTES, as well as the salt pump and the salt heat exchanger for the SHTES, which are fixed) are first identified. The costs included in Table 3.3 are estimated as follows. For SHTES, Herrmann et al. (2004) used a solar salt unit cost of $0.46/kg. Today, this is generally regarded as a low estimate, hence a minimum cost of $0.50/kg is specified. The maximum unit cost for solar salt is $1.50/kg, which is near the $1.74/kg cost identified by Kenisarin (2010). In lieu of more specific information, the cost of the PCM for LHTES is taken to be the same as for the SHTES solar salt. The unit cost of carbon steel, used to calculate the cost of the heat transfer channels and thermosyphons, ranges from $0.80/kg (the current market price for bulk carbon steel) (Steelonthenet.com, 2011) to $2.20/kg, which is the price used by Kelly and Kearney (2006). Although the shells of the thermosyphons are fabricated of carbon steel, the cost of carbon steel has been decoupled

from the cost of the thermosyphon for portions of the following analysis since additional thermosyphon costs are involved. The unit cost of the thermosyphons is varied between $3.00/TS for the minimum cost to $6.00/TS for the maximum cost. Unit costs for the thermosyphons are derived from the material costs (shell, working fluid, and wick), along with estimated manufacturing costs (welding).

Table 3.3: Material unit cost ranges for major cost contributors to both SHTES and LHTES

Material	Minimum Cost ($/Unit)	Average Cost ($/Unit)	Maximum Cost ($/Unit)
Solar Salt (SHTES)	0.50	1.00	1.50
PCM (LHTES)	0.50	1.00	1.50
Carbon Steel	0.80	1.50	2.20
Thermosyphon	3.00	4.50	6.00

A *preliminary cost analysis* is initially conducted to determine the approximate influence of various physical parameters on the overall capital cost of the energy storage systems. From the preliminary analysis, a set of desirable dimensions and parameters are identified, using the approach outlined in Section 3.4. Using these dimensions and parameters, a *sensitivity analysis* is then performed to estimate the influence of various costs noted in Table 3.3. Since neither the preliminary cost analysis nor the sensitivity analysis provides an optimized LHTES design, a LHTES system's ultimate cost is expected to be substantially less than reported here.

3.5.1. Preliminary Cost Analysis

The base case parameters used in the preliminary cost analysis (identified from a number of initial simulations) are included in Table 3.4. Table 3.5 summarizes the required size of the LHTES storage unit and number of thermosyphons for a 9 hour storage period for 50 and 10 MW_e CSP plants, using the base case values of Table 3.4. The overall model suggests that a HTF channel of width W_{chan} = 1.0 m and height H_{chan} = 0.08 m is appropriate, as is a HTF mass flow rate per channel of $\dot{m}_{HTF}$ = 2 kg/s. Likewise, the preliminary cost analysis ultimately suggests that a thermosyphon of diameter D_{TS} = 0.024 m and length L_{TS} = 0.58 m is economically-competitive, so those base case values are reported in Table 3.4. Using these dimensions, a HTF channel length of 44.9 m is required (Table 3.5). For 50MW_e output, a storage system that is 28.6 m wide and 13.6 m tall is appropriate, containing approximately 30,000 metric tons of PCM and 3.3 million thermosyphons. A smaller, 10MW_e system would require the same storage container length due to energy balance and heat transfer considerations, however its width and height would be less than that of the 50 MW_e unit. The mass of PCM and the number of

thermosyphons are reduced in proportion to the power output. For comparison, a 9 hour, 50MW$_e$ SHTES system as reported by Herrmann et al. (2004), has two very large cylindrical storage tanks, each approximately 45 m in diameter and 14 m high, each of which intermittently house a total of 42,000 tons of solar salt. Hence, the LHTES reduces the required overall tank volume by approximately 65%, and reduces the TES medium mass by approximately 30%.

Table 3.4: Base case parameters

Parameter	Base Case Value
HTF Channel Height (H_{chan})	0.08 m
HTF Channel Width (W_{chan})	1.0 m
HTF Channel Mass Flow Rate ($\dot{m}_{HTF}$)	2 kg/s
Thermosyphon Length (L_{TS})	0.58 m
Thermosyphon Diameter (D_{TS})	0.024 m
Storage Time	9 h

Table 3.5: LHTES with thermosyphons for 9 hour storage capacity

Electric Power Capacity	Container Length (m)	Container Width (m)	Container Height (m)	PCM Mass (ton)	Thermosyphon Number
50 MW	44.9	28.6	13.6	30,000	3,300,000
10 MW	44.9	14.3	5.5	6,000	660,000

Table 3.6 presents a comparison between the estimated capital costs of the LHTES (with thermosyphons) and a SHTES (Herrmann et al., 2004) for a $50MW_e$ unit with 9 hour storage (see Table 3.3), using the minimum costs identified in Table 3.3 (thermosyphon unit cost is coupled to the carbon steel cost for this portion of the study, giving a unit thermosyphon cost of $3.40). Note that the minimum costs of Table 3.3 are used in order to be consistent with the study of Hermann et al. (2004) which utilized a low solar salt cost estimate. Overall, the LHTES system is estimated to have an approximate capital cost of $36 MM, compared with $42 MM for a SHTES system. Most of the savings is associated with reduced expenditures for the energy storage medium and the storage container (Table 3.6, lines 1 and 2). However, LHTES has two capital costs which do not exist for SHTES; the thermosyphons, and the HTF channels (Table 3.6, lines 3 and 4). But, the SHTES requires a molten salt-HTF heat exchanger and molten salt pumps ($7 MM, Table 3.6, lines 5 and 6). In addition the SHTES requires operation of salt pumps (550 kW), meaning SHTES has an additional operating cost relative to LHTES (Herrmann et al., 2004). In total, the economic calculations suggest that at least 15% capital cost savings over SHTES can be realized using an LHTES design.

Table 3.6: Capital costs for LHTES and two-tank SHTES (Herrmann et al., 2004)

Equipment	LHTES Cost (US$ MM)	SHTES Cost (US$ MM)
Energy Storage Material*	14.9	21.0
Storage Container	4.8	10.4
Thermosyphons	11.1	-
HTF Channels	1.6	-
Molten Salt Heat Exchanger	-	5.4
Molten Salt Pump	-	1.6
Overhead (10%)	3.3	3.9
Total	35.7	42.3

*Required mass of LHTES salt is 30,000 tons. Total SHTES salt inventory required is 42,000 tons (Herrmann et al., 2004). Heat capacity of SHTES solar salt is calculated to be 127.7 kJ/kg, based upon a liquid specific heat of 1.5 kJ/kg·K and a temperature difference of 85 K (Herrmann et al., 2004).

Figure 3.5 includes the estimated capital cost of LHTES and SHTES for different storage periods, based upon 50MW$_e$ output using the base case values. As the storage time increases, the difference in capital cost between SHTES and the proposed LHTES grows larger, due to the increased mass of the energy storage materials required. Therefore, this particular LHTES design may be more useful for large scale energy storage with a long storage time.

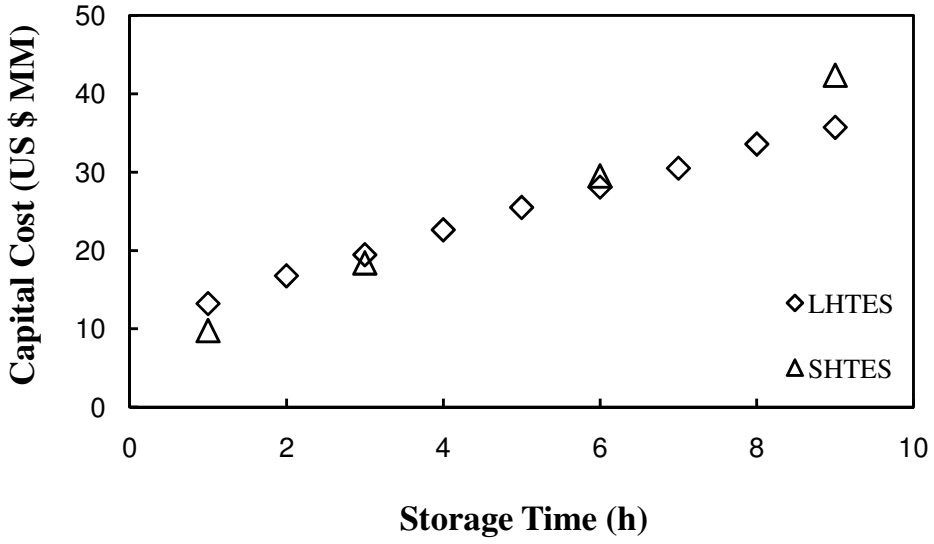

Figure 3.5: Capital costs for the LHTES compared with a SHTES for different storage times. The power generation is 50MW$_e$.

3.5.1.1 Influence of HTF Channel Dimensions and HTF Mass Flow Rate

Figure 3.6 shows the dependence of the LHTES cost on the HTF channel height, HTF channel width, and HTF flow rate per HTF channel. As the height of the HTF channel, H_{chan}, is increased with all other parameters held at their base case values (Fig. 3.6a), the capital cost of the LHTES system increases modestly, whereas when the width of the channel, W_{chan}, is increased with all other parameters at their base case values (Fig. 3.6b) the cost decreases. Therefore, it is concluded that HTF channels with $W_{chan}/H_{chan} > 1$ are desirable. In essence, large, flat HTF channels provide more area for insertion of thermosyphons. From the parametric study, it is found that HTF channels of approximately 0.08 m in height and 1 m in width (identified as open symbols in the figures; the same as the base case values) lead to desirable performance and cost competitiveness.

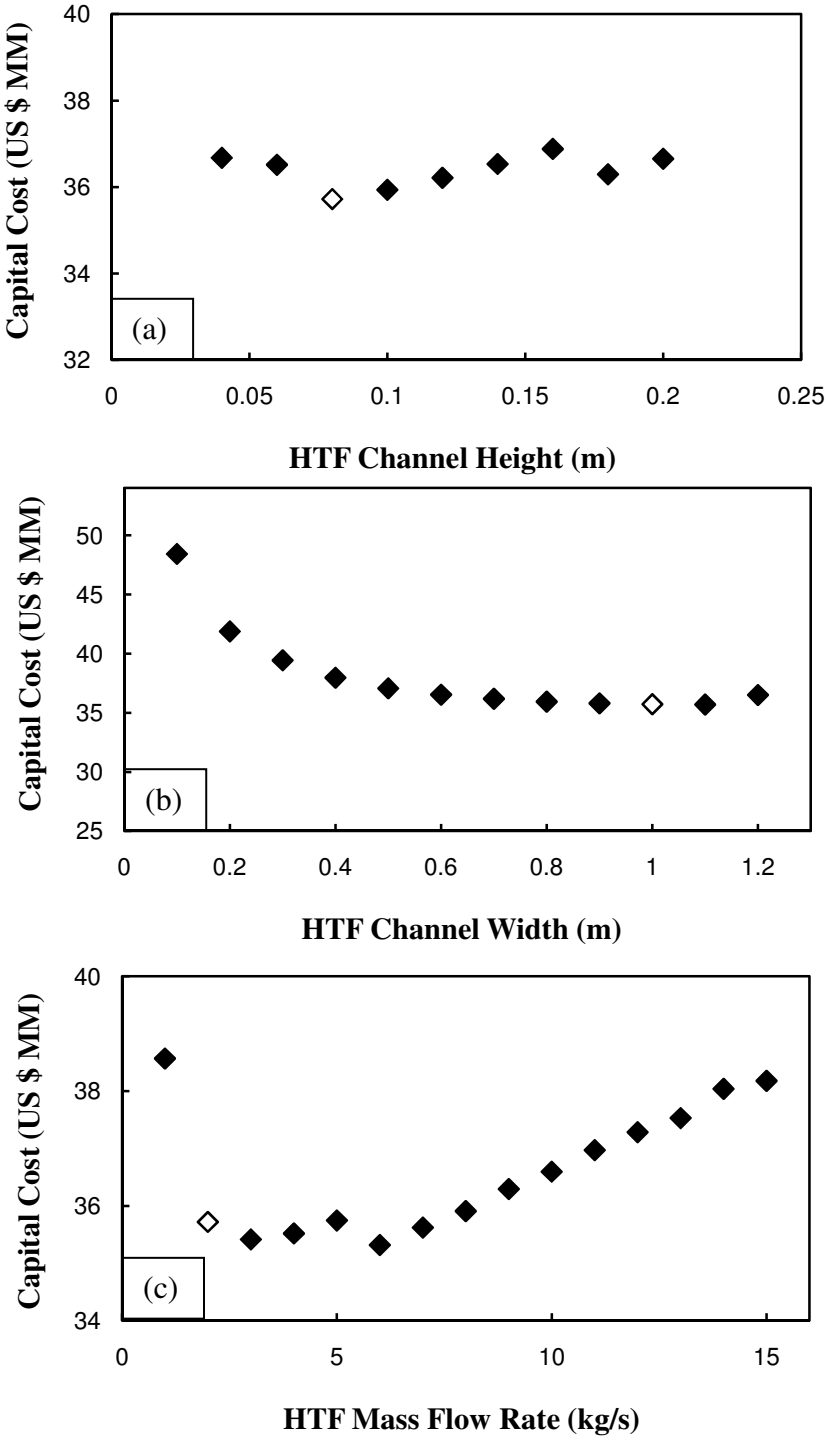

Figure 3.6: LHTES capital cost dependence on (a) HTF channel height, (b) HTF channel width, and (c) HTF mass flow rate. The white diamonds represent base case conditions.

The HTF mass flow rate per channel also impacts the capital cost of the LHTES. Figure 3.6c shows the sensitivity of the capital cost for the proposed LHTES design to the HTF mass flow rate, with all other parameters at their base case values. High mass flow rates correspond to smaller increases in the HTF fluid temperature per unit HTF channel length and, in turn, longer storage tanks. This increases storage container and storage foundation costs. On the other hand, lower HTF flow rates lead to shorter, more numerous HTF channels which can be stacked in the vertical direction, reducing the overall cost. Again, the base case value is identified as the open symbol.

3.5.1.2 Influence of Thermosyphon Dimensions

The thermosyphons are crucial in promoting effective heat transfer between the PCM and the HTF. Figure 3.7a shows the influence of the thermosyphon diameter on the capital costs. As D_{TS} increases with all other parameters at their base case values (wall thickness is kept at 2 mm), the cost of the LHTES increases steadily. Although lower costs are associated with the smaller diameter thermosyphons, the number of thermosyphons increases beyond the already large number associated with the selected values. A thermosyphon diameter of approximately 0.024 m is used as the base case in this study to reduce the required number of thermosyphons, keeping overall costs down. Note however, that larger diameter thermosyphons may be needed if different working fluids are considered in order to avoid the sonic limit for operation (Faghri, 1995).

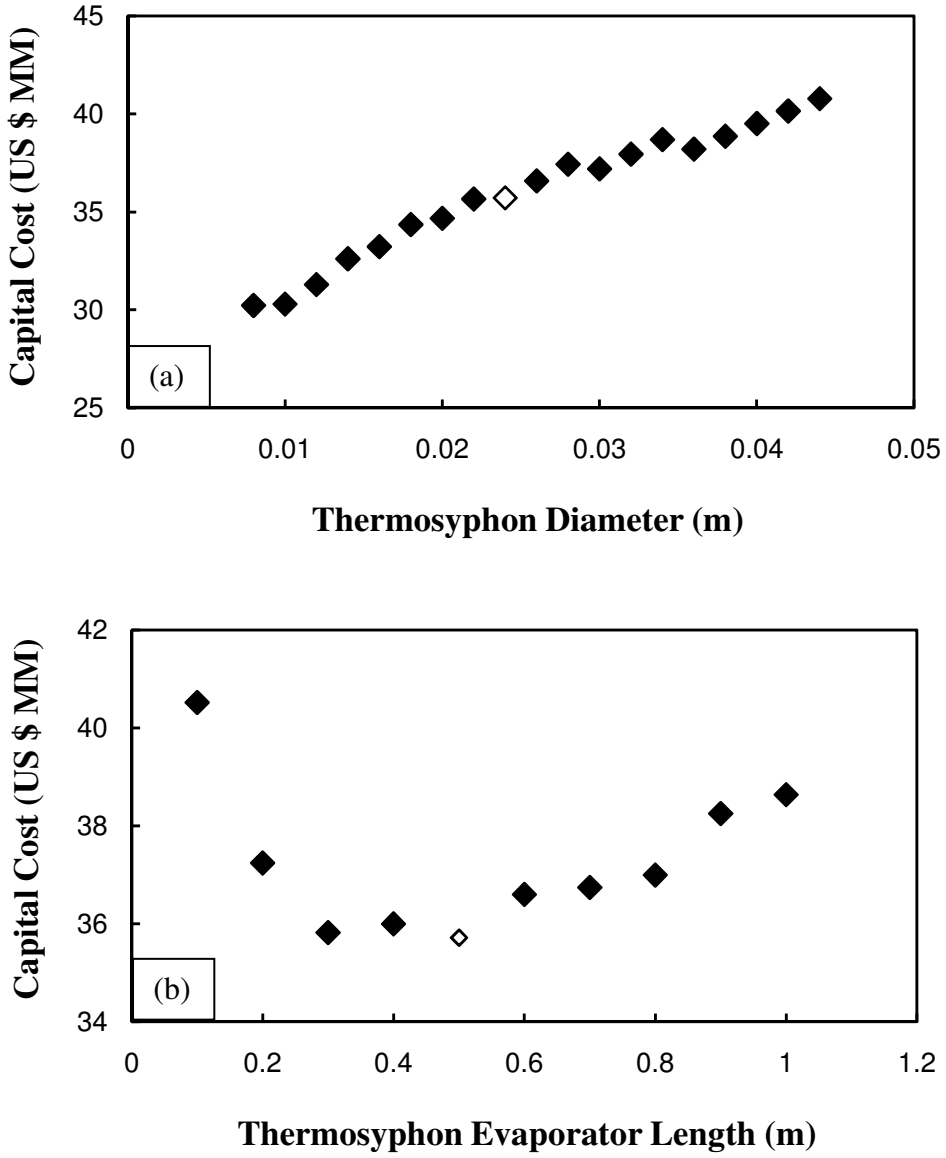

Figure 3.7: LHTES capital dependence on (a) thermosyphon diameter, and (b) thermosyphon evaporator length. The white diamonds represent base case conditions.

The thermosyphon length also influences overall cost, and an optimum thermosyphon length is suggested (Fig. 3.7b). An optimum length exists because a very short thermosyphon occupies volume that would otherwise be taken by PCM that could be solidified by the cold HTF channel surface. Hence, an expense is incurred with little benefit by using short thermosyphons. Alternatively, the heat transfer through a thermosyphon of any length includes a thermal resistance associated with forced convection between the HTF and the condenser section of the thermosyphon. Beyond a certain length, adding more thermosyphon surface area (i.e. increasing the thermosyphon length) becomes ineffective since the thermosyphon heat transfer rate begins to be limited by the forced convection thermal resistance between the HTF and the condenser. Ideally, the distance vertically and horizontal between HTF channels would be maximized within cost and heat transfer limitations to allow for a greater volume of PCM within the storage container. From the preliminary cost analysis, a thermosyphon evaporator length of 0.5 m (0.58 m total length) represents the lowest cost configuration.

3.5.2. Sensitivity Analysis

The preliminary analysis has focused on the influence of geometrical and operating parameters on the overall cost of the LHTES system, assuming fixed values for various unit costs. However, since unit costs of the solar salt, PCM, thermosyphons, and carbon steel are inexact and subject to change, results of a sensitivity analysis are presented in this section. Again, the price ranges for the major cost components in SHTES and LHTES are provided in Table 3.3. Note that thermosyphon costs have been decoupled from carbon steel costs in this part of the study.

3.5.2.1. Impact of PCM, Thermosyphon, and Carbon Steel Unit Price on Overall LHTES Capital Cost

In the results reported in Fig. 3.8, all unit costs are either the minimum or maximum values of Table 3.3, except for the single quantity being varied along the abscissa. Figure 3.8a shows the estimated LHTES capital cost as the PCM unit cost is varied between $0.50/kg and $1.50/kg. The SHTES capital cost using the minimum (maximum) solar salt cost of Table 3.3 is represented by the solid (dashed) lines. For a LiCl/KCl PCM, a unit price of approximately $0.75/kg is the break-even point when the bases of comparison are the minimum cost values of Table 3.3. Alternatively, when the comparison is made using the maximum costs of Table 3.3, the LHTES system is always less expensive than the SHTES system.

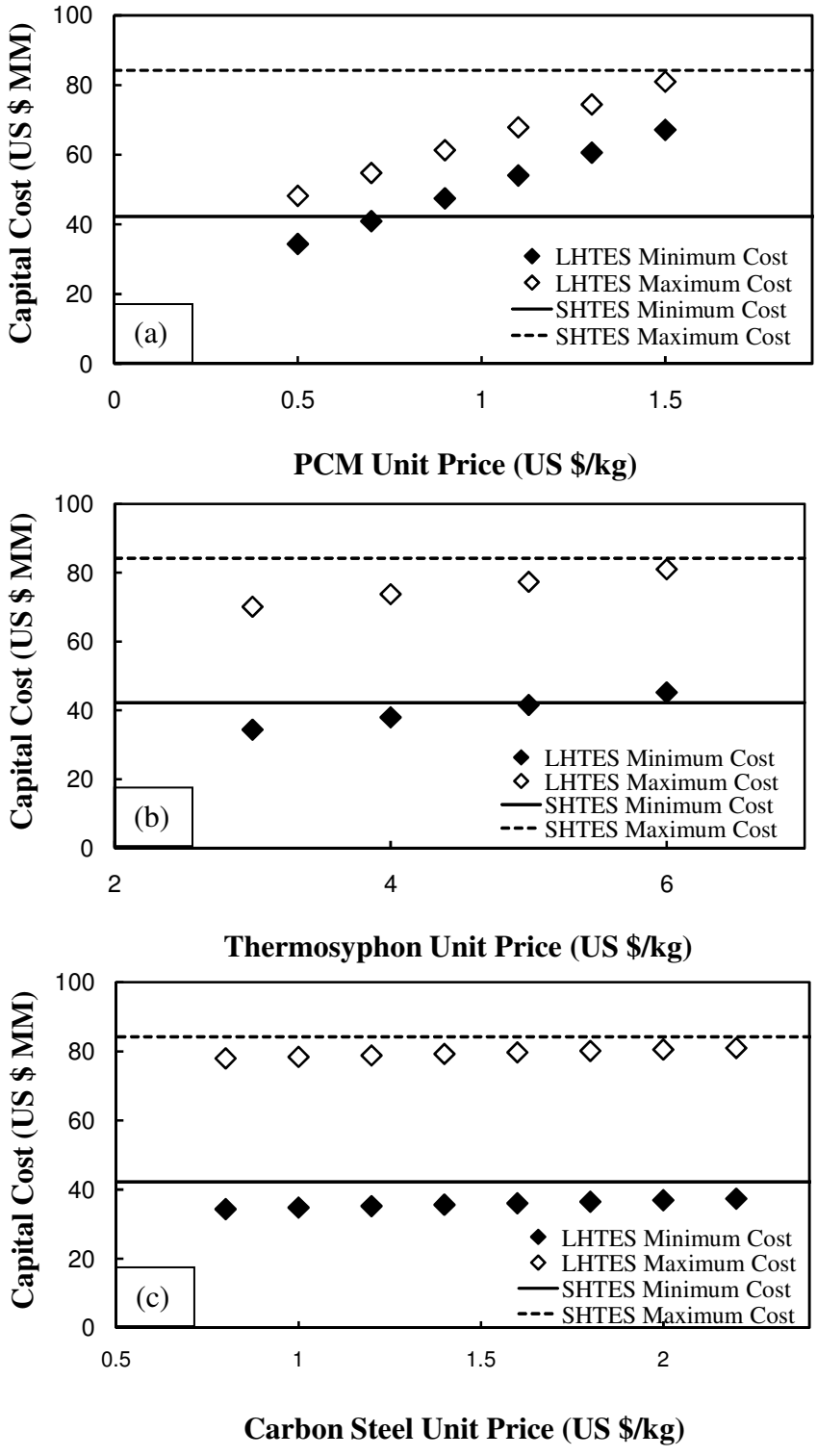

Figure 3.8: Minimum and maximum LHTES and SHTES capital cost with various (a) PCM unit costs (b) thermosyphon unit costs and (c) carbon steel unit cost.

The impact of the thermosyphon unit cost is shown in Fig. 3.8b. LHTES with embedded thermosyphons remains economically competitive with a comparable minimum cost SHTES system for thermosyphon unit costs up to approximately $5. Alternatively, when maximum costs are used in the comparison, the LHTES cost is less than that of the SHTES cost over the entire range of TS cost considered. It is also noted that, in many applications, fins or other extended surfaces are utilized to enhance heat transfer (Bergman et al., 2011). However, thermosyphons are often cost-competitive with solid metallic fins of the same exterior dimensions, due to their hollow interior which reduces metal usage (Toth et al., 1998). Moreover, it has been shown that heat pipes thermally outperform fins in a LHTES (Robak et al., 2011). Since thermosyphons are potentially less expensive than fins and perform better thermally, it is concluded that thermosyphons can offer an important advantage over fins from both the economic and heat transfer perspectives.

The effect of carbon steel cost on LHTES capital cost is shown in Fig. 3.8c. As the price of carbon steel increases from $0.80/kg to $2.20/kg, the LHTES capital cost slowly increases toward the SHTES capital cost scenarios. Even at $2.20/kg, the LHTES capital cost remains below that of the SHTES, suggesting that the cost of carbon steel within the LHTES does not have a large influence on the total capital cost relative to the thermosyphon and PCM components.

5.2.2. Low and High Cost Scenarios for LHTES and SHTES

Table 3.7 provides a summary of the capital costs for the low, average, and high unit price scenarios of Table 3.3. The lowest capital cost LHTES system is

approximately $34 MM (slightly lower than the value listed in Table 3.6 since the thermosyphon unit cost is decoupled from carbon steel cost in this portion of the analysis), compared with $42 MM for SHTES, a difference of approximately 20%. For the average and high cost scenarios listed in Table 3.3, the differences between LHTES and SHTES decrease to approximately 8% and 4%, respectively.

Table 3.7: Minimum, maximum, and average capital cost scenarios for SHTES and LHTES

Storage Type	Minimum Capital Cost ($ MM)	Average Capital Cost ($ MM)	Maximum Capital Cost ($ MM)
SHTES	42	63	84
LHTES	34	58	81

Although the results of Fig. 3.8 and Table 3.7 suggest that LHTES is not as economically attractive under high cost scenarios, it is reiterated that the LHTES system designs considered here have not been optimized. Therefore, the cost reductions achievable through use of the LHTES with thermosyphons, which is already significant under low-cost scenarios, will become larger as optimized LHTES designs are identified.

3.6. Conclusions

A new LHTES design has been proposed to reduce the size and amount of materials needed for TES in CSP. Using a thermal network model, it was shown that while accounting for the difference in the Rankine cycle efficiency between the various designs, a large scale LHTES system utilizing embedded thermosyphons can be cost competitive with two-tank SHTES systems. Potentially, a 15% reduction in capital cost might be realized for the proposed LHTES over the corresponding SHTES. It should be emphasized that the LHTES system with thermosyphons considered here does not represent an optimized design and that, ultimately, cost reductions could be significantly greater than reported in this study.

A wide variety of different PCMs and thermosyphons could be adapted to the proposed LHTES concept outlined in this study. For example, the PCM considered here may require use of metal such as stainless steel to minimize the effects of corrosion, increasing the cost of the thermosyphons. Hence, some combinations will increase the LHTES capital costs, but others may reduce LHTES capital costs beyond those reported here. Use of cascaded LHTES systems with finned thermosyphons based on the proposed LHTES concept has the potential to further reduce the amount of PCM and

construction materials through better utilization of the energy storage capacity of PCMs at different melting temperatures. Finally, long-term corrosion and weld reliability testing for the LHTES system with thermosyphons is warranted.

Nomenclature

C	free convection constant
D	diameter
c_p	specific heat
E_t	thermal energy
Fo	Fourier number, $\alpha_s t/H_s^2$
g	gravitational acceleration
h	heat transfer coefficient
H	height
k	thermal conductivity
L	length
m	mass
$\dot{m}$	mass flow rate
n	free convection constant
Nu	Nusselt number, hH_ℓ/k_ℓ
Ra	Rayleigh number, $g\beta\Delta TH_\ell^3/\nu_\ell\alpha_\ell$
Ste	Stefan number, Eqs. 2.1 and 2.5
t	time, thickness
T	temperature
W	width

Greek Symbols

α	thermal diffusivity
β	thermal expansion coefficient
ε	effectiveness

η	efficiency
λ	latent heat of fusion
ν	kinematic viscosity
ρ	density

Subscripts

BM	benchmark
c	charging
chan	channel
crit	critical
dc	discharging
e	electric
f	final
Fin	fin
HP	heat pipe
HTF	heat transfer fluid
HX	heat exchanger
i	initial
in	inlet
ℓ	liquid
LH	latent heat
LS	large scale
m	melt
mod	module

out	outlet
PCM	phase change material
s	solid
SS	small scale
TS	thermosyphon
∞	ambient

Superscripts

i	index
n	summation limit
~	modified value

References

References

Agyenim, F., Eames, P., Smyth, M., "Heat transfer enhancement in medium temperature thermal energy storage system using a multitube heat transfer array," *Renewable Energy*, vol. 35, pp. 198-207, 2010.

Alibaba.com, Minerals and metallurgy products, 2011, < http://www.alibaba.com/Minerals-Metallurgy_p9>, (Last accessed 6.13.11).

Balikowski, J.R., Mollendorf, J.C., "Performance of phase change materials in a horizontal annulus of a double-pipe heat exchanger in a water circulation loop," Journal *of Heat Transfer*, vol. 129, pp. 265-272, 2007.

Bathelt, A.G., Viskanta, R., "Heat transfer at the solid-liquid interface during melting from a horizontal cylinder," *International Journal of Heat and Mass Transfer*, vol. 23, pp. 1493-1503, 1980.

Bergman, T.L., Lavine, A.S., Incropera, F.P. DeWitt, D.P., Fundamentals of Heat and Mass Transfer, 7th ed., Wiley, Hoboken, 2011.

Choi, K. J., Hong, J. S., "Experimental studies of melting phenomena from a constant heat flux vertical plate," *Experimental Heat Transfer*, vol. 3, pp. 49-63, 1990.

Faghri, A., Heat Pipe Science and Technology. Taylor & Francis, New York, 1995.

Faghri, A., US Patent No. 5000252, 1991.

Faghri, A., US Patent No. 4976308, 1990.

Figliola, R.S., Beasley, D.E., Theory and Design for Mechanical Measurements, fourth ed., Wiley, Hoboken, pp. 148-190, 2006.

References

Fukai, J., Kanou, M., Kodama, Y., Miyatake, O., "Thermal conductivity enhancement of energy storage media using carbon fibers," *Energy Conversion and Management*, vol. 41, pp.1543-1556, 2000.

Hale Jr., N.W., Viskanta, R., "Solid-liquid phase change heat transfer and interface motion in materials cooled or heated from above or below," *International Journal of Heat and Mass Transfer*, vol. 23, pp. 283-292, 1980.

Hale Jr., N.W., Viskanta, R., "Photographic observation of the solid-liquid interface motion during melting of a solid heated from an isothermal vertical wall," *Letters in Heat and Mass Transfer*, vol. 5, pp. 329-337, 1978.

Herrmann, U., Kelly, B., Price, H., "Two-tank molten salt storage for parabolic trough solar power plants," *Energy*, vol. 29, pp. 883-893, 2004.

Ho, C.-J., Viskanta, R., "Inward solid-liquid phase-change heat transfer in a rectangular cavity with conducting vertical walls," *International Journal of Heat and Mass Transfer*, vol. 27, pp. 1055-1065, 1984.

Ju, Y., Yuan, Z., Chen, Z., "Experimental study of melting heat transfer in an enclosure with three discrete protruding heat sources," *Journal of Thermal Science*, vol. 7, pp. 111-118, 1998.

Kelly, B., Kearney, D., "Thermal storage commercial plant design for a 2-Tank indirect molten salt system," *National Energy Renewable Laboratory*, NREL/SR-550-40166, pp. 1-32, 2006.

References

Kenisarin, M.M., "High-temperature phase change materials for thermal energy storage," *Renewable and Sustainable Energy Reviews*, vol. 14, pp. 955-970, 2010

Lacroix, M., "Numerical simulation of a shell-and-tube latent heat thermal energy storage unit," *Solar Energy*, vol. 50, pp. 357-367, 1993.

Laing, D., Bahl, C., Bauer, T., Lehmann, D., Steinmann, W.-D., "Thermal energy storage for direct steam generation," *Solar Energy*, vol. 85, pp. 627-633, 2011.

Lee, W.-S., Chen, B.-R., Chen, S.-L., "Latent heat storage in a two-phase thermosyphon solar water heater," *Journal of Solar Energy Engineering*, vol. 128, pp. 69-76, 2006.

Liu, Z., Wang, Z., Ma**,** C., "An experimental study on heat transfer characteristics of heat pipe heat exchanger with latent heat storage. Part I: Charging only and discharging only modes," *Energy Conversion and Management*, vol. 47, pp. 944-966, 2005.

Madaeni, S.H., Sioshansi, R., Denholm, P., "How thermal energy storage enhances the economic viability of concentrating solar power," *Proceedings of the IEEE*, vol. 100, pp. 335-347, 2011.

Medrano, M., Yilmaz, M.O., Nogués, M., Martorell, I., Roca, J., Cabeza, L.F., "Experimental evaluation of commercial heat exchangers for use as PCM thermal storage systems," *Applied Energy*, vol. 86, pp. 2047-2055, 2009.

Michels, H., Pitz-Paal, R., "Cascaded latent heat storage for parabolic trough solar power plants," *Solar Energy*, vol. 81, pp. 829-837, 2007.

References

Mills, D., "Advances in solar thermal electricity technology," *Solar Energy*, vol. 76, pp. 19-31, 2004.

Miner, K., Ploski, D., Hiraoka, D., Personal Communication. Pratt & Whitney Rocketdyne, 2010.

Moran, M.J., Shapiro, H.N., Boettner, D.D., Bailey, M.B., Fundamentals of Engineering Thermodynamics, 7th ed., John Wiley and Sons, Hoboken, 2011

Robak, C.W., Bergman, T.L., Faghri, A., "Enhancement of latent heat energy storage using embedded heat pipes," *International Journal of Heat and Mass Transfer*, vol. 54, pp. 3476-3484, 2011a.

Robak, C.W., Bergman, T.L., Faghri, A., "Economic evaluation of latent heat thermal energy storage using embedded thermosyphons for concentrating solar power applications," *Solar Energy*, vol. 85, pp. 2461-2473, 2011b.

Shabgard, H., Bergman, T.L., Sharifi, N., Faghri, A., "High temperature latent heat thermal energy storage using heat pipes," *International Journal of Heat and Mass Transfer*, vol. 53, pp. 2979-2988, 2010.

Sparrow, E.M., Larson, E.D., Ramsey, J.W., "Freezing on a finned tube for either conduction-controlled or natural-convection-controlled heat transfer," *International Journal of Heat and Mass Transfer*, vol. 2, pp. 273-283, 1981.

SSAB, Welding cost calculator, 2011, <http://www.ssab.com/en/Brands/Domex/Products/Steelfacts/Calculate-welding-costs/>, (Last accessed 3.15.11).

References

Steelonthenet.com, 2011 World prices for steel, 2011, <http://www.steelonthenet.com/price_info.html>, (Last accessed 6.8.11)

Toth, J., DeHoff, R., Grubb, K., "Heat Pipes: The Silent Way to Manage Desktop Thermal Problems," *Intersociety Conference on Thermal Phenomena*, pp.449-455, 1998.

Velraj, R., Seeniraj, R. V., Hafner, B., Faber, C., Schwarzer, K., "Heat transfer enhancement in a latent heat storage system," *Solar Energy*, vol. 65, pp. 171-180, 1999.